PL-TR--91-3068
Vol. 1 of 3

PL-TR--91-3068
Vol. 1 of 3

EXPERIMENTAL DETERMINATION OF MECHANICAL PROPERTIES FOR A CARBON-CARBON COMPOSITE:

VOLUME 1.

R.A. Heller
S. Thangjitham
T. Rantis
T.G. Heller

Department of Engineering Science and Mechanics
Virginia Polytechnic Institute and State University
Blacksburg VA 24061-0219

April 1992

Final Report

APPROVED FOR PUBLIC RELEASE; DISTRIBUTION UNLIMITED.

92

PHILLIPS LABORATORY
Propulsion Directorate
AIR FORCE SYSTEMS COMMAND
EDWARDS AIR FORCE BASE CA 93523-5000

NOTICE

When U.S. Government drawings, specifications, or other data are used for any purpose other than a definitely related Government procurement operation, the fact that the Government may have formulated, furnished, or in any way supplied the said drawings, specifications, or other data, is not to be regarded by implication or otherwise, or in any way licensing the holder or any other person or corporation, or conveying any rights or permission to manufacture, use or sell any patented invention that may be related thereto.

FOREWORD

This Final 3 Volume Report was prepared by the Department of Engineering Science and Mechanics, Virginia Polytechnic Institute and State University, Blacksburg VA, under contact F04611-87-K-0010 for Operating Location AC, phillips Laboratory (AFSC), Edwards AFB CA 93523-5000. OLAC PL Project Manager was Chi T. Liu.

This report has been reviewed and is approved for release and distribution in accordance with the distribution statement on the cover and on the SF Form 298.

CHI T. LIU
Project Manager

BERNARD E. WILKERSON, CAPT, USAF
Chief, Propellants Branch

WAYNE L. PRITZ
Director,
Components Engineering Division

RANNEY G. ADAMS
Public Affairs Director

REPORT DOCUMENTATION PAGE

Form Approved
OMB No. 0704-0188

1. AGENCY USE ONLY (Leave blank)	2. REPORT DATE	3. REPORT TYPE AND DATES COVERED
	April 1992	Technical Report 5/1/87—6/30/91

4. TITLE AND SUBTITLE
Experimental Determination of Mechanical Properties for a Carbon/Carbon Composite: A Probabilistic Method to Establish the Reliability of Carbon/Carbon Rocket Motor Nozzles

5. FUNDING NUMBERS
C: F04611-87-K-0010
PR: 3059
TA: 004G

6. AUTHOR(S)
R. A. Heller, S. Thangjitham, T. Rantis and T. G. Heller

7. PERFORMING ORGANIZATION NAME(S) AND ADDRESS(ES)
Department of Engineering Science and Mechanics
Virginia Polytechnic Institute and State University
Blacksburg, VA 24061—0219

8. PERFORMING ORGANIZATION REPORT NUMBER

9. SPONSORING/MONITORING AGENCY NAME(S) AND ADDRESS(ES)
Department of the Air Force, OLAC, Phillips Lab (AFSC)
Edwards AFB, CA 90523—5000
Dr. C. T. Liu, OLAC PL/RCP

10. SPONSORING/MONITORING AGENCY REPORT NUMBER
PL—TR—91—3068
Final Report Part I

11. SUPPLEMENTARY NOTES
This is the first part of a three part final report.

COSATI Codes: 07/02; 13/08

12a. DISTRIBUTION/AVAILABILITY STATEMENT
Public Release; Distribution Unlimited

12b. DISTRIBUTION CODE

13. ABSTRACT *(Maximum 200 words)*

Mechanical property characterization experiments have been carried out on a 2—D, woven, carbon—carbon composite. These were followed by tests to determine statistical variability and size effects. Tension, compression, in plane and interlaminar shear tests, unnotched and notched four point beam and plate (with and without holes) tests were performed. Weibull distribution parameters are reported.

14. SUBJECT TERMS
Carbon—Carbon, 2D Woven Composite, Reliability, Weibull Distribution, Mechanical Properties, Size Effect, Experiments.

15. NUMBER OF PAGES
76

16. PRICE CODE

17. SECURITY CLASSIFICATION OF REPORT	18. SECURITY CLASSIFICATION OF THIS PAGE	19. SECURITY CLASSIFICATION OF ABSTRACT	20. LIMITATION OF ABSTRACT
Unclassified	Unclassified	Unclassified	SAR

TABLE OF CONTENTS

LIST OF TABLES

LIST OF FIGURES

INTRODUCTION

Carbon–carbon composites consisting of two dimensional woven fabric layers of carbon fibers imbedded in a carbon matrix are of great interest in high temperature structural applications. Though the material is brittle, unlike metals, it retains its strength at elevated temperatures.

As in the case with other composite materials the quality of larger components can not be controlled as carefully as that of small laboratory specimens. As a consequence a "size effect" is present in carbon–carbon resulting in reduced strengths for full size structures. Because imperfections, such as matrix poor regions, dicontinuous fibers, porosity, etc. are statistically distributed throughout the component, size effect is treated with the aid of statistically based theories.

The probability of the existence of larger imperfections is greater in large components than in laboratory samples. The probability of failure increases, therefore, with the size of the component as well as with the magnitude of the applied stresses.

The "weakest link" principle together with the Weibull distribution is utilized to calculate the reliability of components based on specimen data. Basic experiments have been performed in order to characterize the materials. To validate analytical results involving size effect, specimens of widely varying sizes would have to be tested. Such tests are, however, impractical both from a material cost point of view and due to the unavailability of large capacity test equipment.

An approach has been devised to circumvent this problem. Specimens with and without stress concentrations are tested. In specimens with stress raisers only a small volume is highly stressed while specimens without such concentrations have a larger volume stressed. In this manner stressed volume ratios of the order of 1000:1 may be achieved in the laboratory.

Because the material has different properties in three orthogonal directions: warp and fill in the plane of the laminae, and across the plies[1], a large number of tests were performed to obtain statistically meaningful properties in tension, compression and shear.

Size effect was ascertained on small notched and unnotched beam specimens while the analysis was validated on larger plate and beam specimens containing holes and notches respectively.

DESCRIPTION OF THE MATERIALS

Two–dimensionally woven carbon–carbon plates were received, courtesy of HITCO. The plates measuring nominally 10×6½×¼ inches, were obtained in two batches. The first shipment consisting of five panels were numbered as follows:

1 – 30028515
2 – 30027963
3 – 30030756
4 – 30034137
5 – 30028760

With warp direction along the length and fill direction along the width.

Construction:	WVA Graphite (Union Carbide), F64 Resin (U.S. Polymerics FM–5064).
Densification:	2 cycles LPI process
Specific Density:	1.51–1.52

The panels have been high temperature pyrolized as follows:

Carbonized at 1000° F
Pyrolized at 4000° F
Carbonized at 1000° F
Pyrolized at 4000° F
Carbonized at 1000° F

Panel No. 5 received a third pyrolization at 4000° F.

The second batch of six panels numbered

6 – 30050245
7 – 30050728
8 – 30050742
9 – 30051018
10 – 30051020
11 – 30051499

were received without any description of treatment. It has been assumed that they were constructed and treated similarly to the first four plates.

The volume fraction of fiber and matrix were not available for any of the panels. These were estimated from microphotographs of the plates presented in Figs. 1 and 2, and from the rule of mixtures discussed in Section 10.

On the basis of these examinations and data presented in Reference 2, the fiber volume fraction was estimated to be 50%. Of these 30% and 20% are respectively in the warp and fill directions, respectively.

The material is modelled as a laminate consisting of alternating matrix filled fiber and pure matrix layers comprising 60% and 40% of laminate thickness. Because the actual volume fraction of pure fibers is only 50%, 10% of matrix material is assumed to be imbedded in the fiber interstices.

Figure 1
Microphotograph of Carbon/Carbon plate showing warp fibers

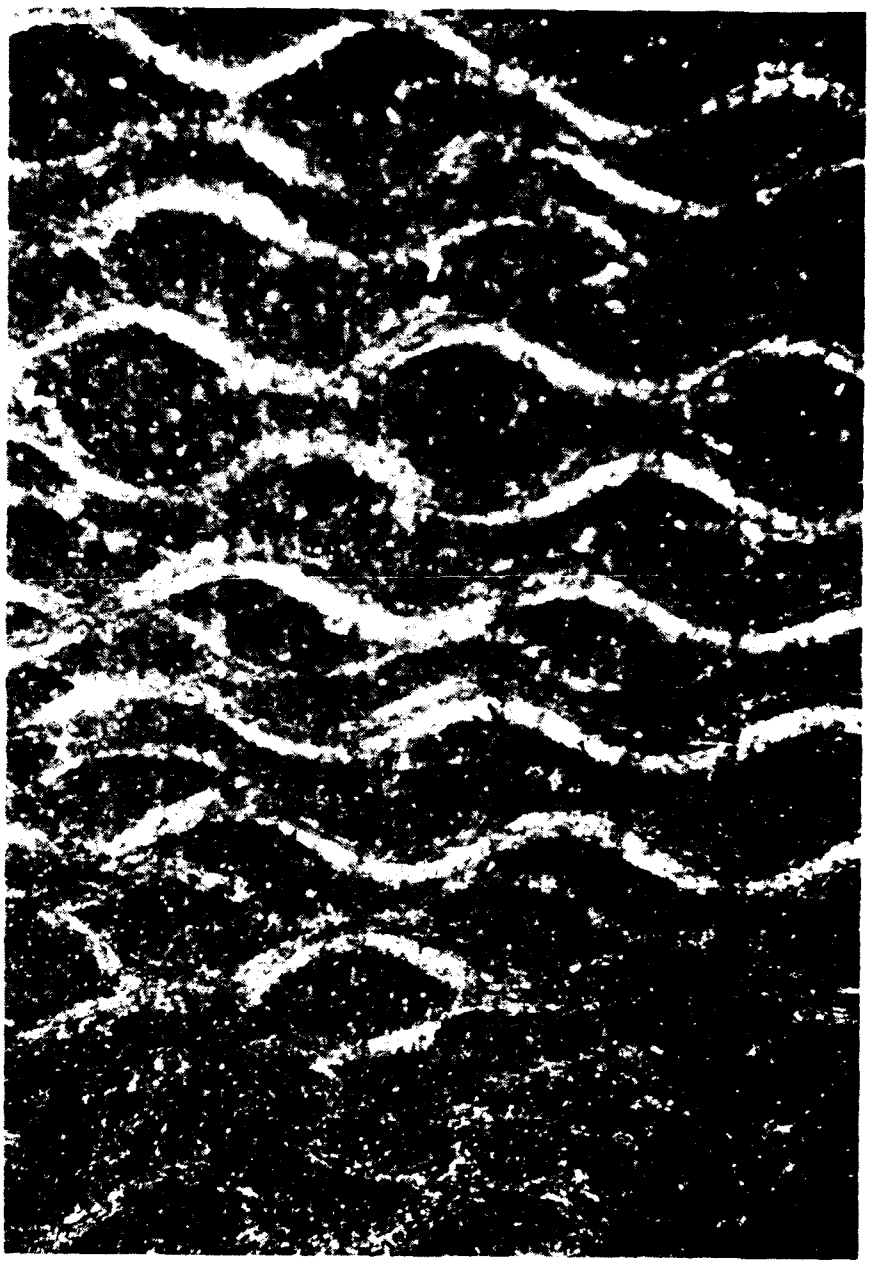

Figure 2
Microphotograph of Carbon/Carbon plate showing fill fibers

Hence, the fiber volume in the fiber layer is 5/6. Considering the 3:2 ratio of fibers in the warp and fill directions, the warp fiber volume fraction, v_{fw}, in the layer becomes

$$v_{fw} = \frac{3}{5} \times \frac{5}{6} = \frac{1}{2}$$

while the fill fiber fraction, v_{fF}, is

$$v_{fF} = \frac{2}{5} \times \frac{5}{6} = \frac{1}{3}$$

The remaining material, $v_{mw} = \frac{1}{2}$ in the warp direction and $v_{mF} = \frac{2}{3}$ in the fill direction, is a "pseudo–matrix", a combination of matrix material and fibers running perpendicular to the warp and fill fibers respectively. It is assumed that fill fibers do not contribute significantly to the modulus or the strength in the warp direction and vice versa.

Using a modulus $E_m = 0.5 \times 10^6$ psi for this pseudo–matrix material the rule of mixtures yields average values for the two moduli, E_{fw} and E_{fF} of the orthotropic fiber layer.

$$E_w = v_{fw}E_{fw} + v_{mw}E_m \quad (1)$$

$$E_f = v_{fF}E_{fF} + v_{mF}E_m \quad (2)$$

where E_w and E_F are the measured moduli of the composite in the two directions, $v_{fw} = \frac{1}{2}$, $v_{mw} = \frac{1}{2}$, $v_{fF} = \frac{1}{3}$ and $v_{mF} = \frac{2}{3}$.

Table 1. DMA and Vibration Tests for Modulus

TYPE OF TEST	NO. OF TESTS	TYPE OF SPECIMEN	TEMP °F	$\bar{E}$ KSI $\times 10^3$	σ_E
VIBRATION	5	1W	RM	1.989	.245
VIBRATION	4	2W	RM	1.979	.149
VIBRATION	5	1W	500	1.972	.227
VIBRATION	4	2W	500	1.984	.160
DMA	3	1W	–180	2.080	.509
DMA	3	1W	RM	1.965	.437
DMA	3	1W	750	1.530	.220
VIBRATION	5	1F	RM	1.019	.177
VIBRATION	2	2F	RM	1.094	
VIBRATION	5	1F	500	1.072	.193
VIBRATION		2F	500	1.066	
DMA	5	1F	–180	1.408	.136
DMA	5	1F	RM	1.297	.136
DMA	5	1F	750	1.047	.187

NONDESTRUCTIVE EXAMINATION OF PANELS

The first five panels were examined in a CT scanner by Aerojet Strategic Propulsion Company. The videotape of this Hertis Inspection indicated various matrix rich and matrix poor regions in the plates.

Because of the scarcity and cost of the materials it was not possible to prepare separate matrix rich or poor specimens. Additionally, the purpose of the project is to establish methods of reliability analysis which take into account such statistical variabilities in the material.

As a consequence these random variations have been considered only in the determination of the statistical means, standard deviations and other distribution parameters. Statistical variations of mechanical properties were also observed through the thickness of the plates (see Section 5).

Nondestructive tests were also performed to determine the elastic modulus of the material. Two types of equipment were used in these experiments.

The Dupont Dynamic Mechanical Analyzer (DMA 983)[3] produces low frequency, small amplitude vibrations at various temperatures and automatically determines and plots the applied frequency and the corresponding elastic or storage modulus, E', as well as the loss modulus E'' of the specimen. The ratio of the two, $E''/E' = \tan \alpha$ is the loss tangent and is indicative of the damping in the material. Specimens for these tests are fixed end beams. Typical plots are shown in Fig. 3 and the averaged data are presented in Table 1.

Cantilever beams were also tested under vibration in an MB shaker. First and second natural frequencies were recorded and the elastic modulus was calculated from these based upon the following relationship[4]:

$$E_n = \omega_n^2 m/\beta_n^4 I \qquad (3)$$

where ω_n is the n^{th} natural frequency, m the mass per unit length, I the moment of inertia and $(\beta L)_1 = 1.875$, $(\beta L_2) = 4.695$. Specimens were .5 in wide, .02 in thick and L = 5.5 and 9.3 in. long.

The data are listed in Table 1. The designations of 1W, 2W, 1F and 2F refer to the orientation of laminae in the specimen. W and F indicate that the longitudinal axes are along the warp (W) or fill (F) direction. In specimens numbered 1, laminae are parallel to the width while in No. 2 they are parallel to the thickness of the sample. The values presented are within the statistical range of the tension and compression test results of Section 4.

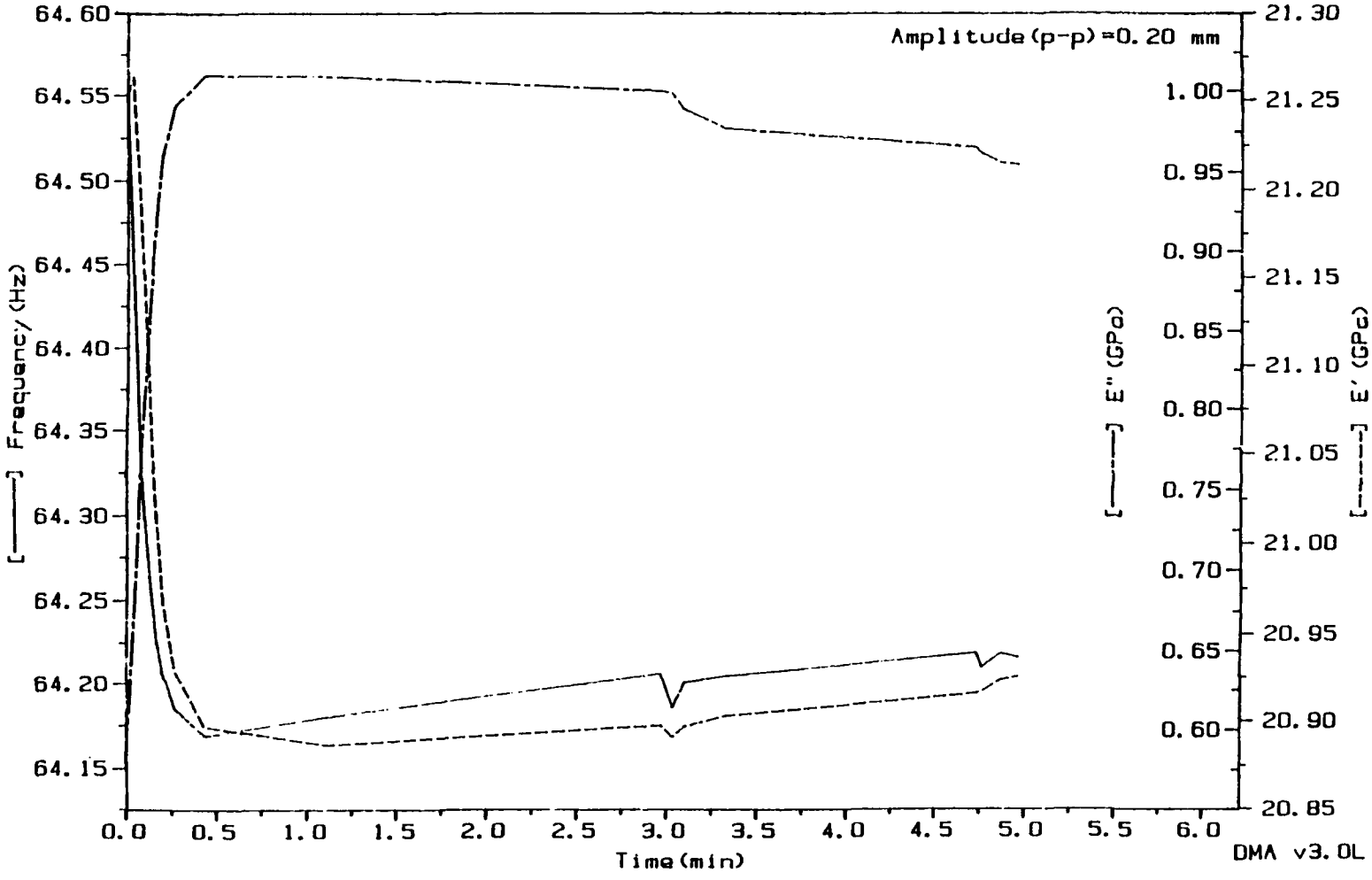

Figure 3
Plot of storage (elastic) modulus, E′, loss modulus, E′′ and natural frequency as functions of time.

TENSION AND COMPRESSION TESTS

To determine the mechanical properties of the material, tension and compression tests were performed in both the warp and fill directions. Off angle tests described in Section 6 were also conducted.

Specimens were cut from the panels described in Section 2; a typical arrangement is presented in Fig. 4. Experiments were performed on dog–bone shaped samples in tension and on prismatic bars in compression. Some specimens were prepared with a cross–ply thickness identical to the plate thickness while in other cases, in an attempt to have a larger number of samples available, thick specimens were sliced into three thin specimens as shown in Fig. 5.

A screw type Instron testing machine was employed to obtain load–deformation data from which stress–strain curves were plotted. Typical curves, in both warp and fill directions, are presented in Figs. 6–9.

Specimens were cut from various plates. Though some differences in results were observed from plate to plate, these differences were small enough to be attributable to statistical dispersion.

Averaged values and standard deviations for modulus, maximum strength and maximum strain are presented in Table 2. The data are consistent with those published in Ref. 1.

While tension specimens failed in most cases at 90 degrees to the longitudinal axis, compression tests produced diagonal shear failures as illustrated in Figs. 10 and 11.

Poisson's ratios were determined in some of the tension tests and are also presented in Table 2.

Table 2. Average Tension and Compression Data

No. of specimens tested	Test direction	Type of test	$\bar{E}$ ksi × 10^3	σ_E ksi × 10^3	$\bar{S}_{max}$ ksi	σ_S ksi	$\bar{\epsilon}_{max}$ in/in × 10^{-3}	σ_ϵ in/in × 10^{-3}	ν_{12}	ν_{31}	ν_{21}	ν_{32}
18	W	T	2.140	.149	13.416	.926	8.500	1.710		.426	.093	
6	F	T	1.188	.277	5.638	.219	9.000	2.959	.048			.203
6	W	C	2.125	.247	8.298	.628	4.366	1.152				
14	F	C	1.501	.260	5.652	.686	6.399	3.212				

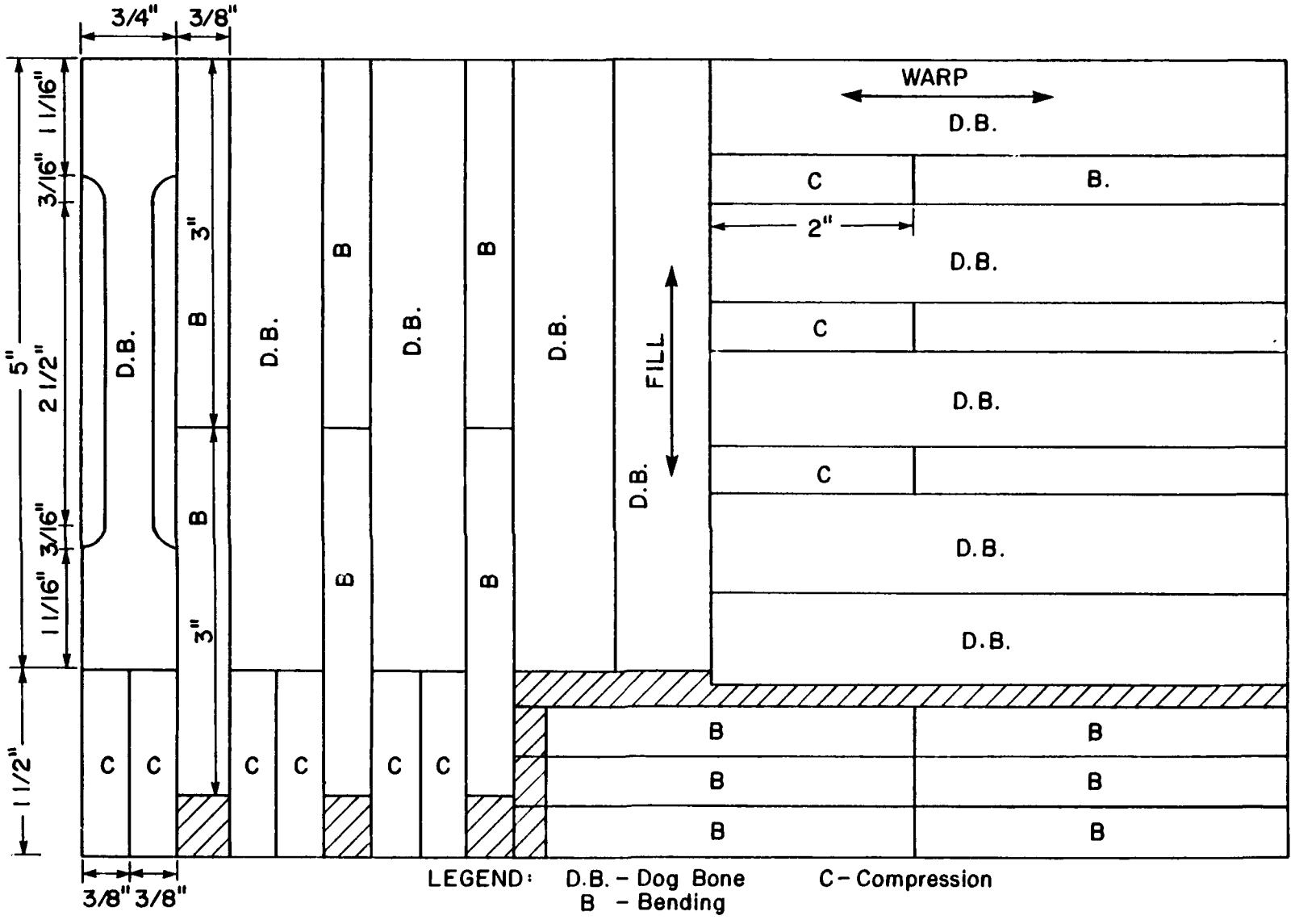

Figure 4
Typical arrangement of specimens cut from a 10×6 1/2×1/2" plate

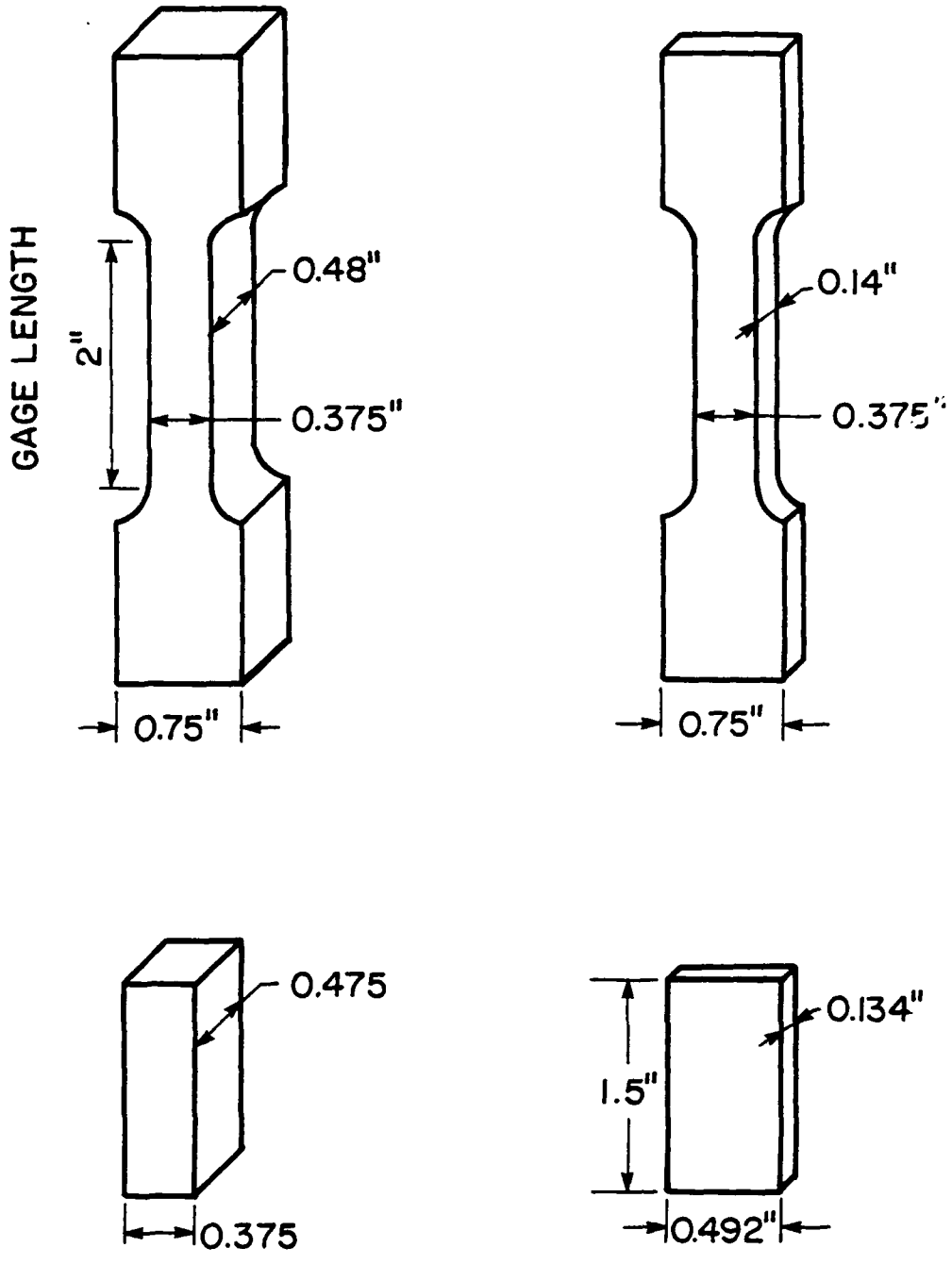

Figure 5
Dimensions of tension and compression specimens

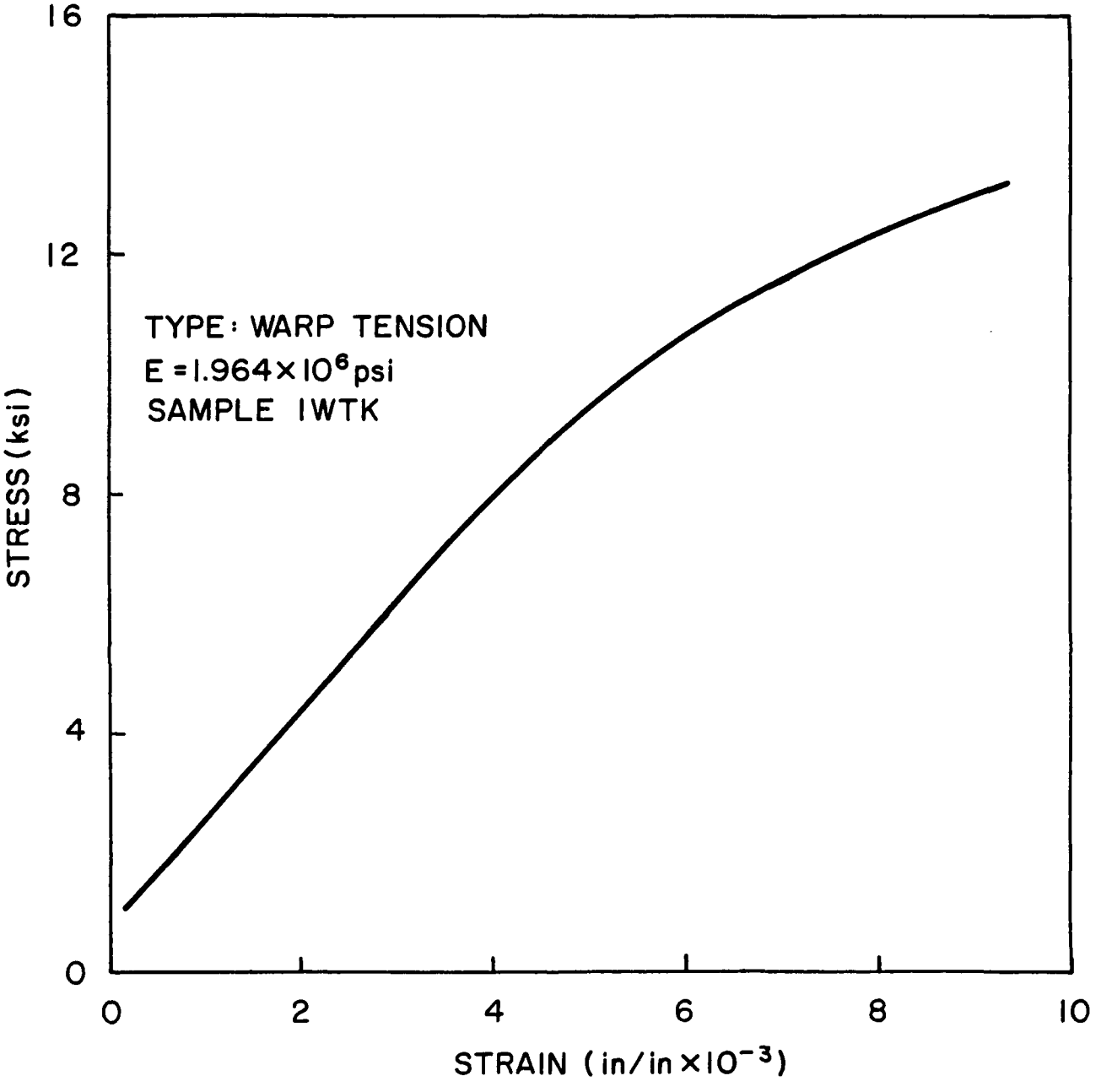

Figure 6
Typical tensile stress–strain curve in the warp direction

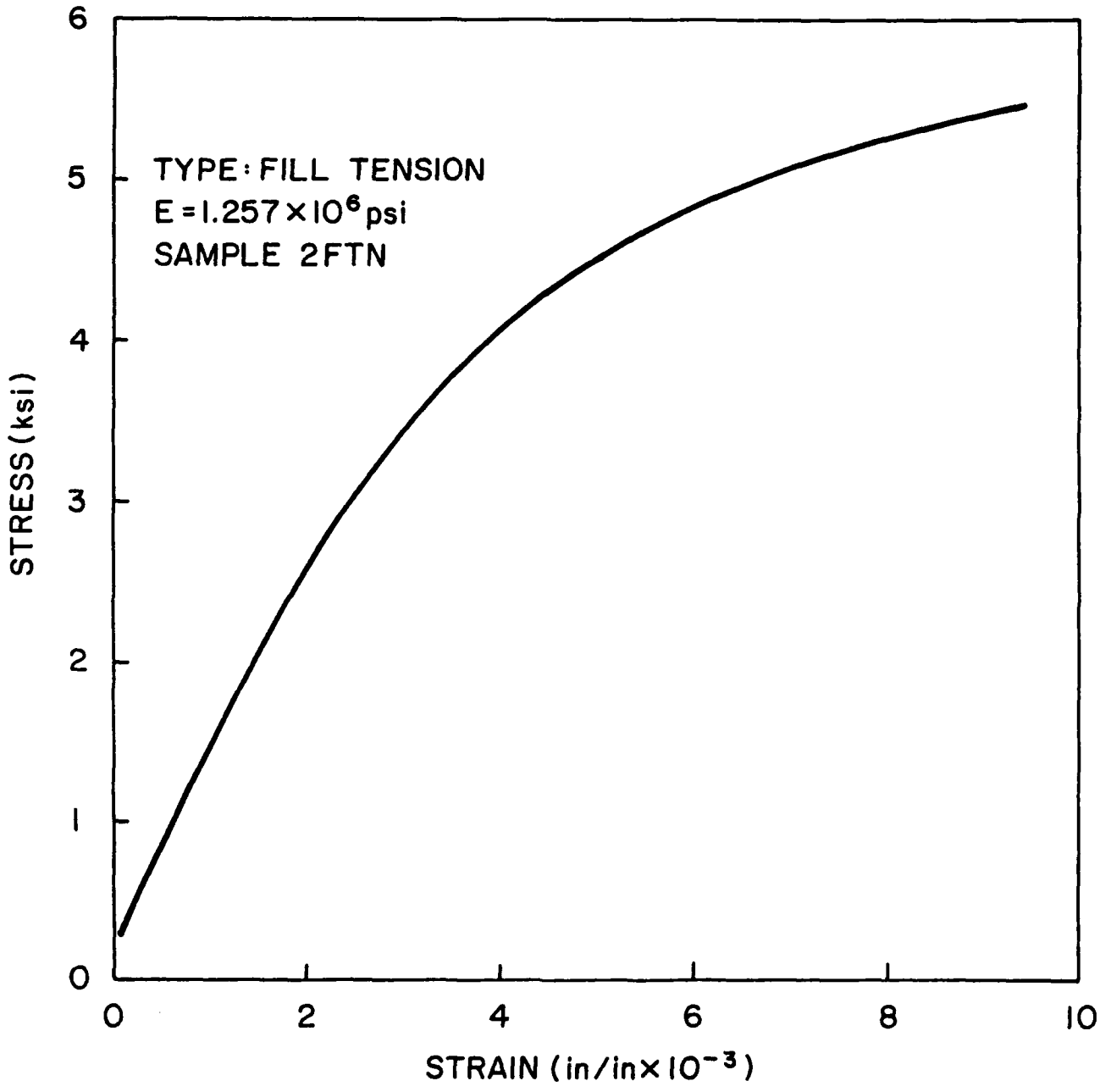

Figure 7
Typical tensile stress–strain curve in the fill direction

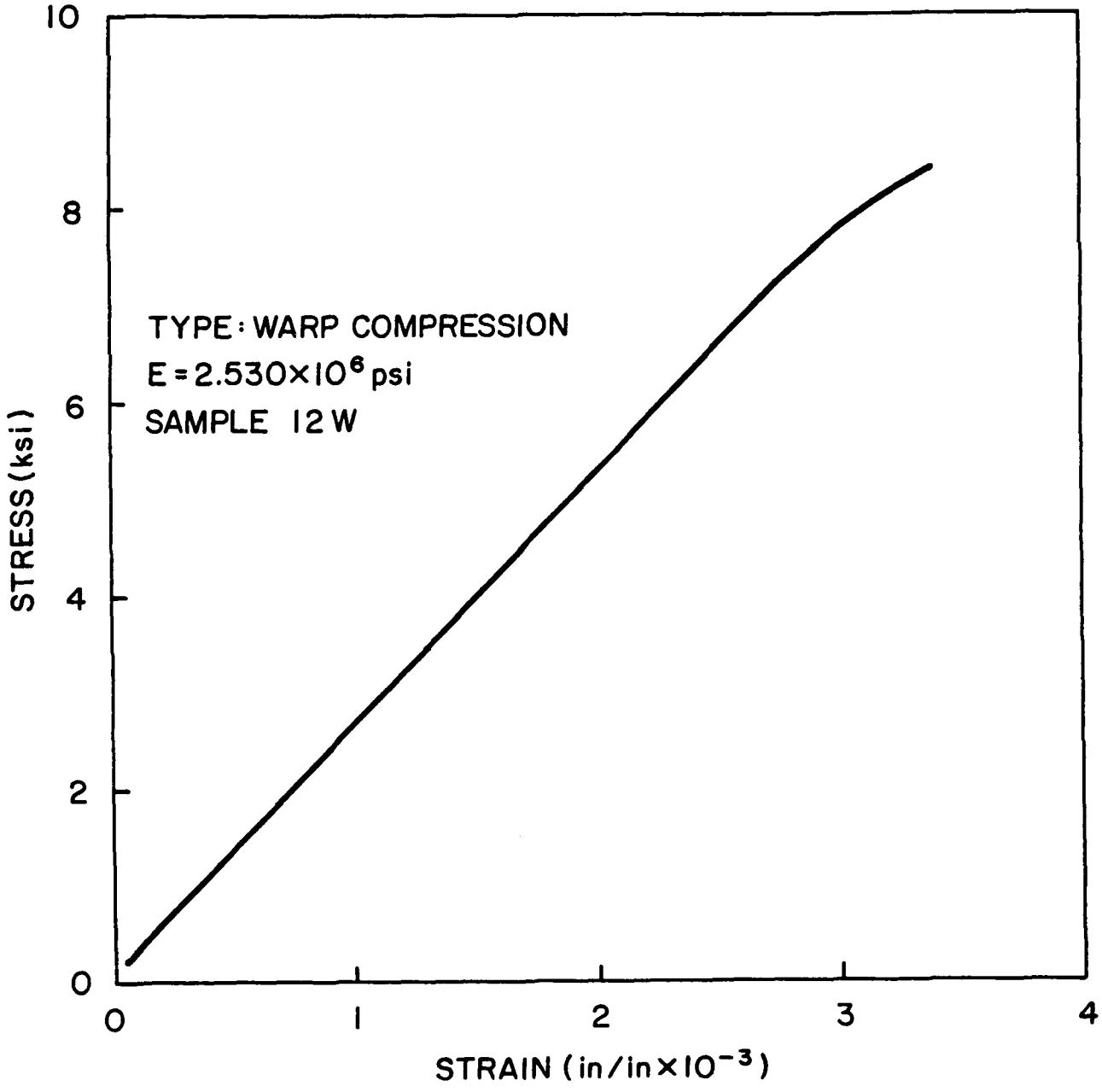

Figure 8
Compressive stress–strain curve for a warp specimen

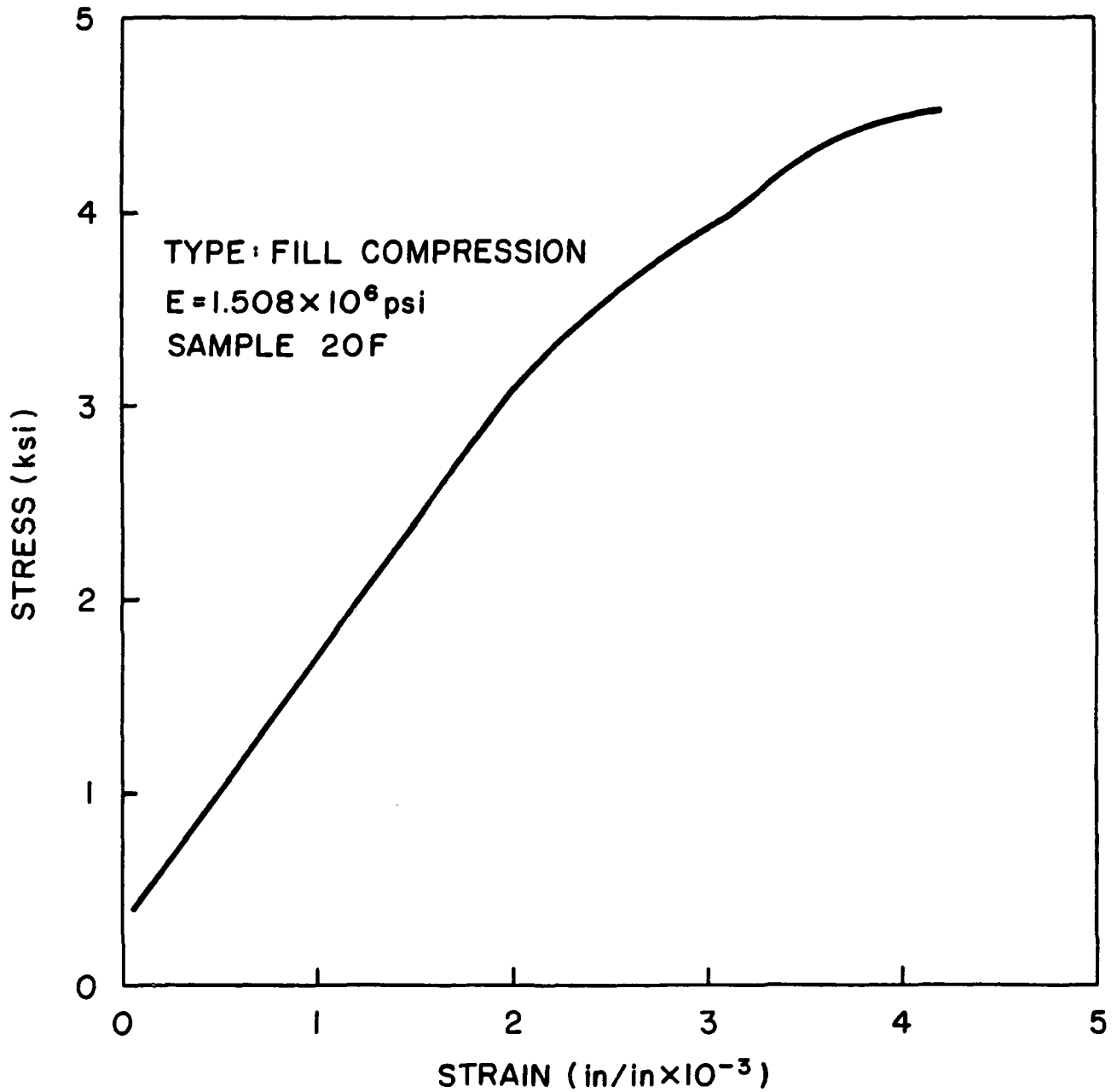

Figure 9
Compressive stress–strain curve for a fill specimen

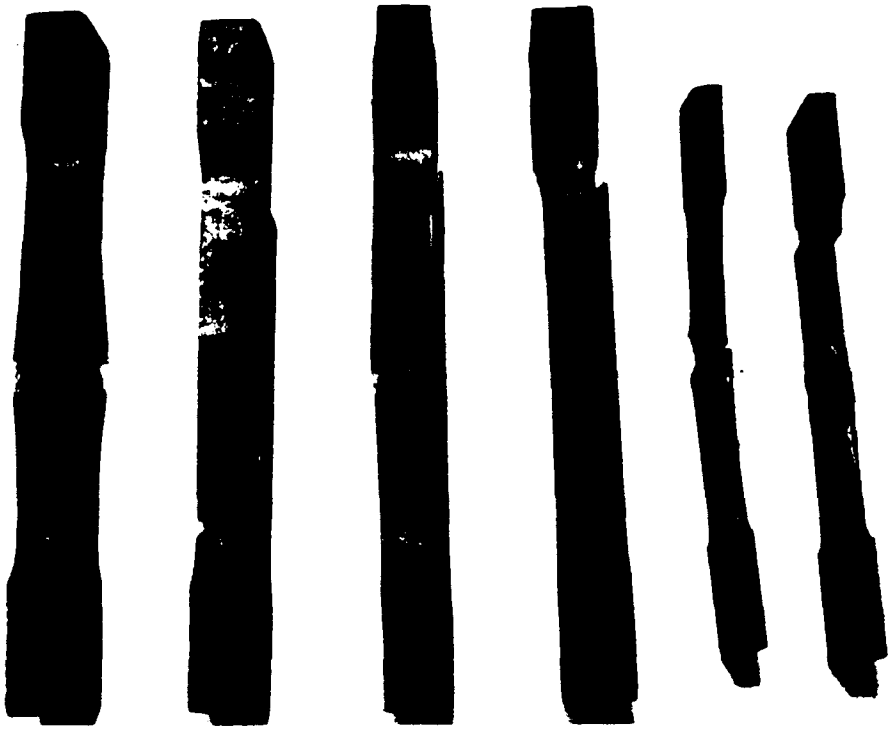

Figure 10
Failed tension specimens

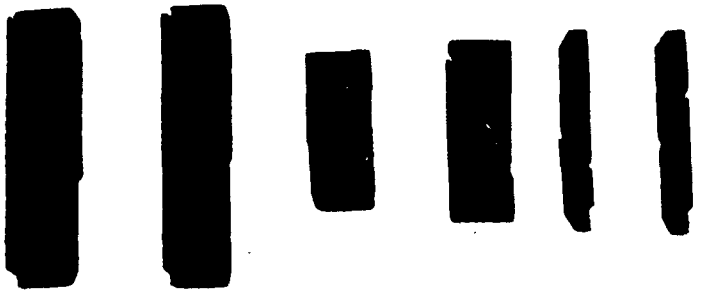

Figure 11
Failed compression specimens

THROUGH THICKNESS VARIATIONS OF PROPERTIES

In order to examine the variability of mechanical properties through the thickness of plates, full thickness specimens were sliced into six layers and tested in tension. The results presented in Table 3 indicate that the top (No. 0) and bottom (No. 5) layers are weaker than specimens taken from mid thickness while the elastic modulus shows an increase from top to bottom.

Because the aim of the present project is to use probabilistic concepts for the establishment of reliability methods in structural analysis, these variations of properties were utilized only in the determination of distribution parameters.

TABLE 3. Thru Thickness Variation of Properties

(Warp Direction)

Sample	E_1 KSI×10^3	σ_{max} KSI	P_{max} lbs	ϵ_{lat} in/in×10^{-3}	ϵ_{ax} in/in×10^{-3}	ν_{21}
0	2.310	3.49	80	.196	1.523	.128
1	2.440	7.30	150	.251	3.050	.086
2	2.515	13.68	255	.350	5.270	.087
3	2.583	10.00	210	.420	4.630	.087
4	2.827	10.42	210	.372	4.260	.108
5	2.885	7.46	140	.313	3.030	.101

OFF AXIS TESTS

Loads applied to structures constructed of the 2D carbon/carbon material may result in multiaxial stress states. Under such conditions the directions of principal stresses do not necessarily coincide with the warp and fill directions. It is, therefore, necessary to examine the strength and other mechanical properties of the materials at various angles to the fiber directions.

One of the panels from the second batch has been cut into dog–bone shaped tension specimens and prismatic compression samples with specimen axes oriented at 0, 15, 30, 45, 60, 75 and 90° to the warp direction as shown in Fig. 12. Samples with the full thickness of the plate have been sliced into three, 0.14 in thick specimens.

Average values of three data and their standard deviations are listed in Table 4a and 4b. The variations of mechanical properties with loading angles are presented in Figs. 13–15.

Average stress–strain curves are plotted in Fig. 13 while in Figs. 14 and 15 the modulus and strength are presented as functions of loading direction.

The failure surface of the tension specimens formed an angle with the loading direction. With the exception of 0° and 15° specimens failure occurred on planes parallel to the warp fibers as indicated in Fig. 16 while 15° specimen failed on a plane nearly parallel to the fill fibers. The specimens failed in shear.

Utilizing the expressions for rotated stress axes

$$\sigma_{x'} = \frac{\sigma_x+\sigma_y}{2} + \frac{\sigma_x-\sigma_y}{2}\cos 2\phi + \tau_{xy}\sin 2\phi \qquad (4)$$

$$\tau_{x'y'} = -\frac{\sigma_x-\sigma_y}{2}\sin 2\phi + \tau_{xy}\cos 2\phi \qquad (5)$$

stresses in the directions of the fibers and the shear stress along the failure surface may be calculated.

An examination of Fig. 17 indicates that the maximum resolved shear strength, R_{wF} = 2750 psi is observed in specimens with a loading direction of 15° to the warp fibers while a minimum R_{Fw} = 1860 psi is calculated for 60° specimens. As a consequence, the shear strength R_{wF} and R_{Fw} could be estimated as R_{wF} = 2750 psi and R_{Fw} = 1860 psi.

These values are, however, low compared with the results of the in–plane shear tests of Section 8.

TABLE 4a. Off–axis Tension Properties

Direction	E E(ksi×10³)	σ_E	S_{max} (ksi)	σ_s	ϵ_{maxax} ($\frac{in}{in}\times10^{-3}$)	σ_ϵ
0°	2.231	0.150	12.578	0.781	8.700	1.200
15°	2.111	0.604	10.835	0.791	11.000	3.000
30°	1.564	0.100	6.898	0.347	13.000	2.000
45°	1.378	0.077	5.333	0.400	14.000	2.000
60°	1.267	0.116	4.471	0.399	14.700	4.000
75°	1.156	0.038	4.524	0.370	9.300	0.580
90°	1.022	0.230	4.462	0.154	18.000	7.000

TABLE 4b. Off–axis Compression Properties

Direction	E E(ksi×10³)	σ_E	S_{max} (ksi)	σ_s	ϵ_{maxax} ($\frac{in}{in}\times10^{-3}$)	σ_ϵ
0°	2.098	0.202	8.620	0.934	11.708	.166
15°	2 088	0.105	8.757	0.010	12.192	0.015
30°	1.518	0.145	7.893	0.006	17.167	0.016
45°	1.290	0.135	6.987	0.009	20.200	0.002
60°	1.215	0.100	6.791	0.001	20.167	0.041
75°	1.275	0.002	6.560	0.008	17.353	0.016
90°	1.448	0.005	6.093	0.008	16.375	0.022

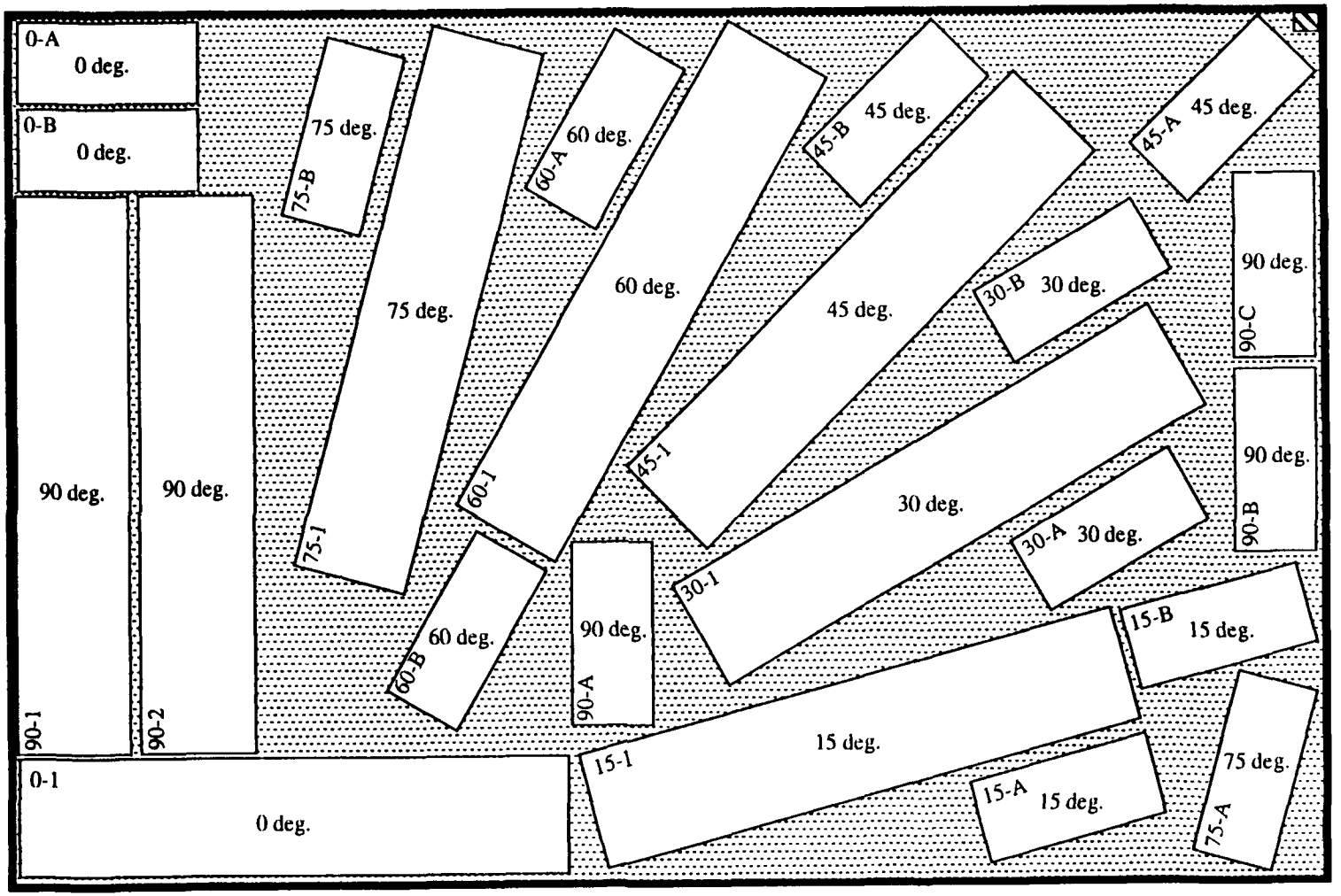

Figure 12
Arrangement of Off–axis test samples in a plate

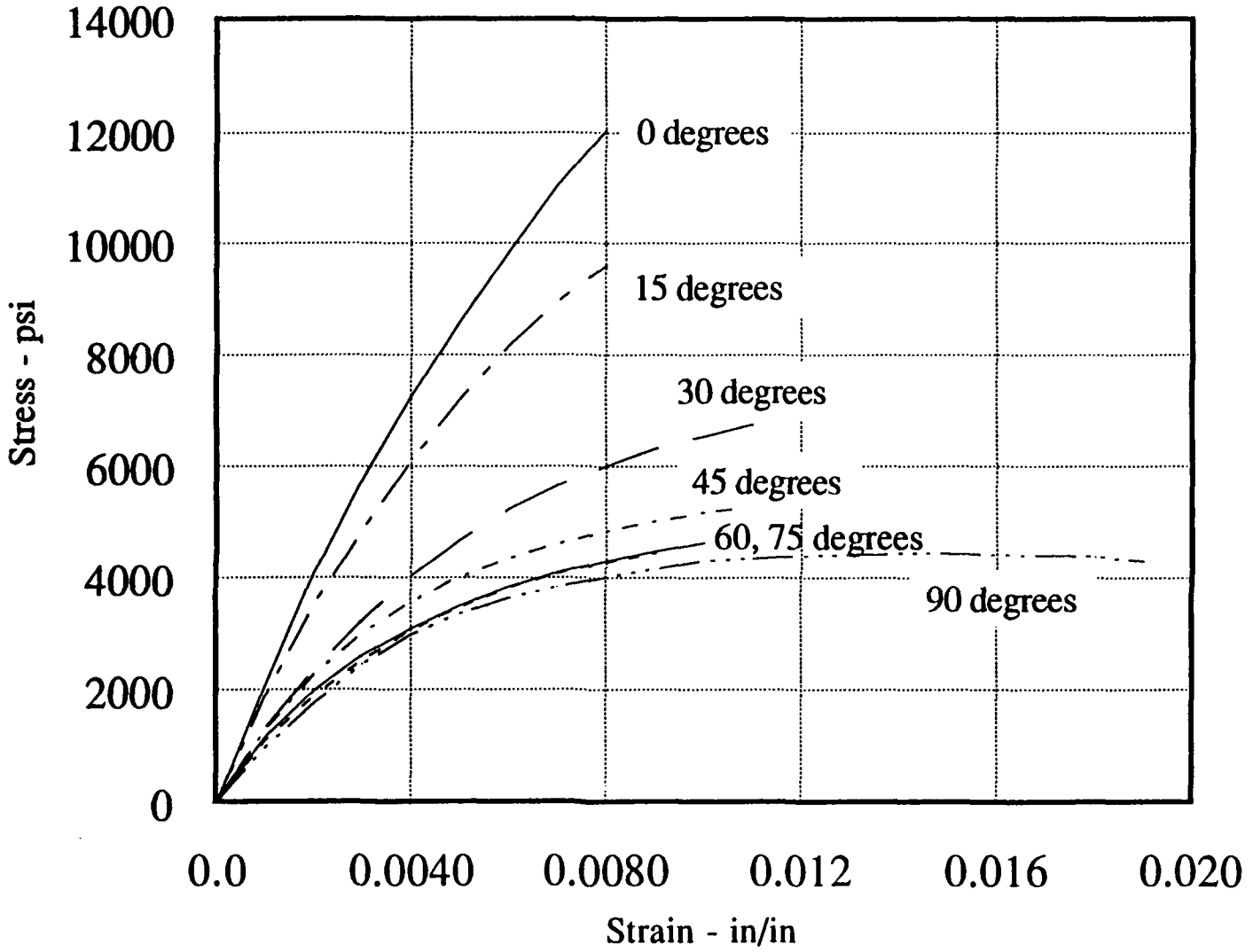

Figure 13
Off–axis tensile stress strain curves

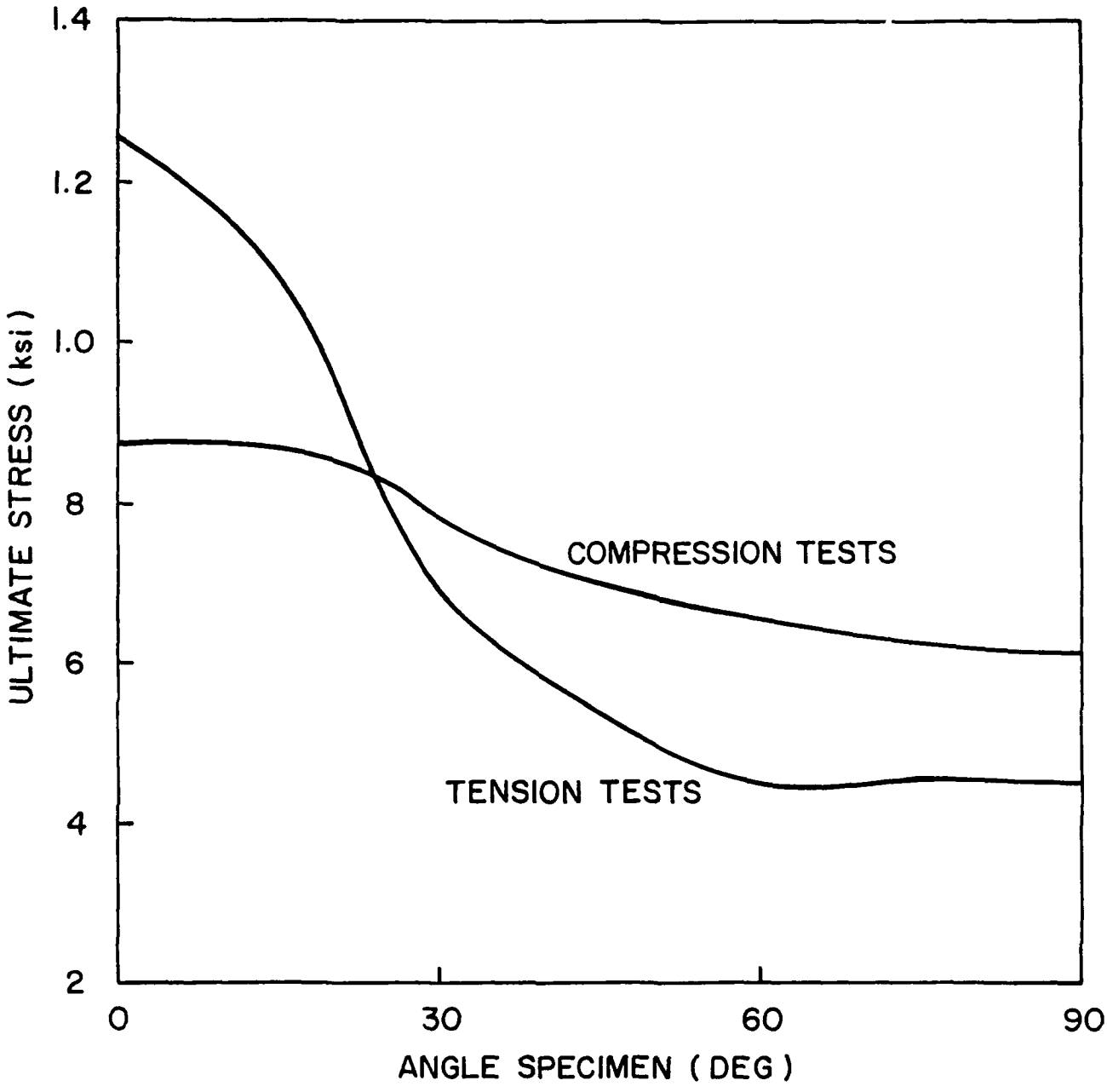

Figure 14
Tension and compression strengths as functions of specimen angles

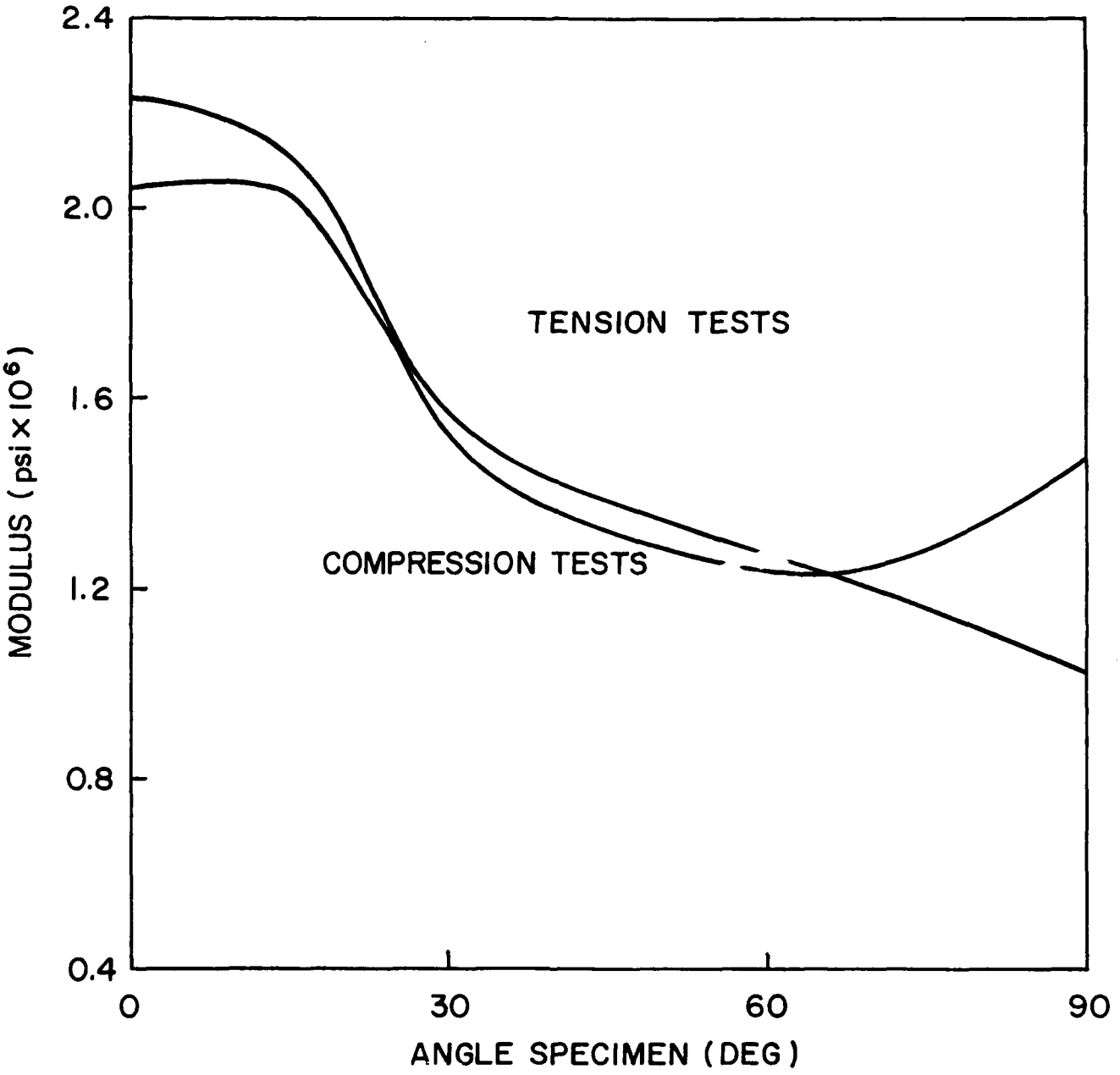

Figure 15
Elastic modulus as a function of specimen angles

Specimen θ	Failure Angle ϕ
0 degrees	90 degrees
15 degrees	120 degrees
30 degrees	30 degrees
45 degrees	45 degrees
60 degrees	60 degrees
75 degrees	80 degrees
90 degrees	90 degrees

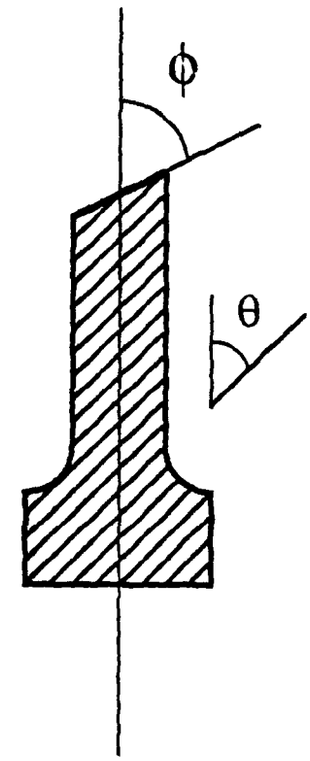

Figure 16
Direction of failure surfaces in Off–axis samples

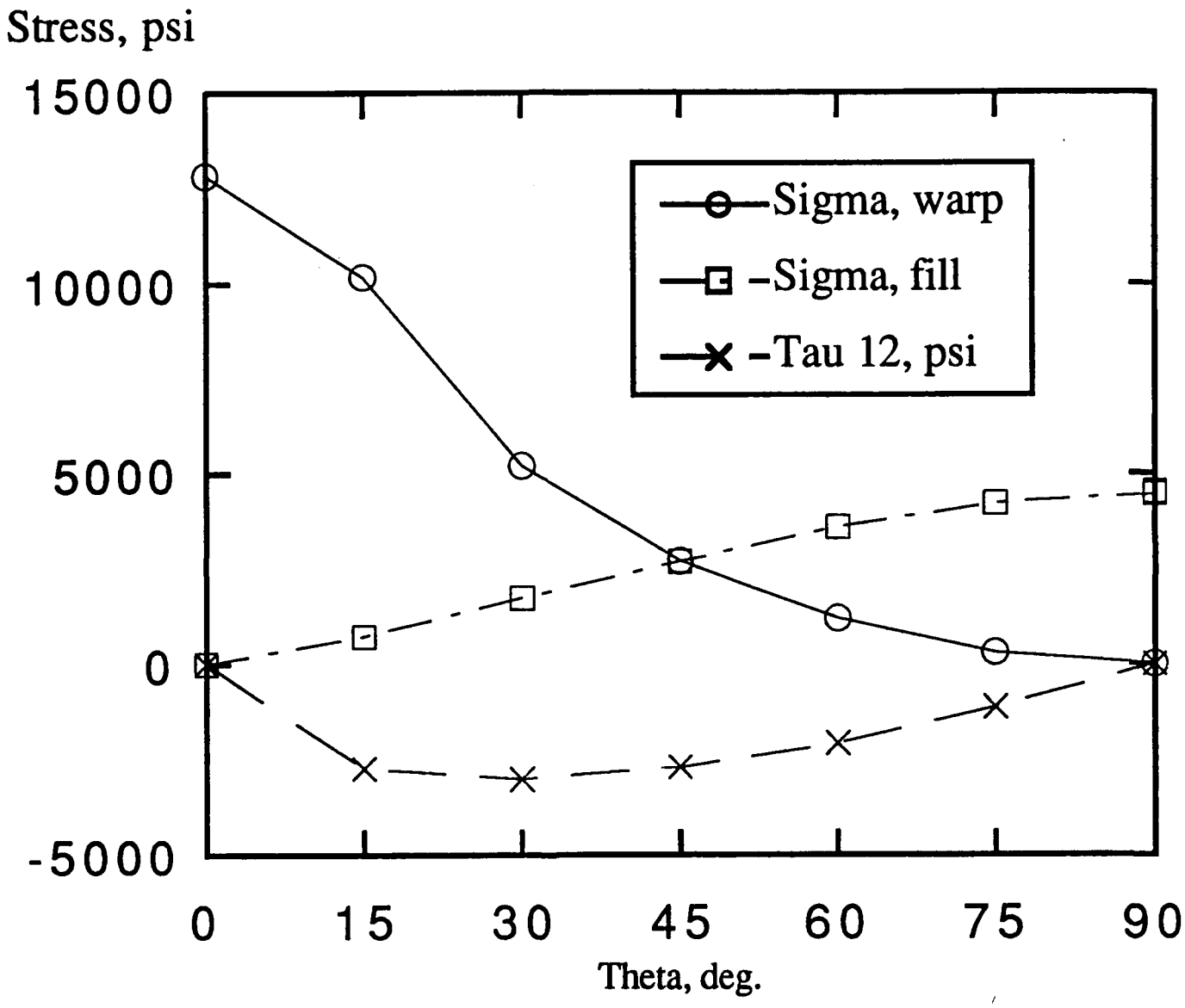

Figure 17
Resolved shear stress, τ_{12}, and tension stresses σ_1, σ_2 as functions of specimens angle

INTERLAMINAR SHEAR TESTS

To determine the interlaminar shear moduli G_{AW} and G_{AF} as well as the interlaminar shear strengths R_{AW} and R_{AF}, where W, F and A refer to warp, fill and cross–ply directions, respectively, specially designed specimens were prepared as shown on Fig. 18. These specimens are similar to those suggested in Ref. 1.

Tests were performed with longitudinal axes parallel to either the warp or the fill directions.

The experiments were carried out in a screw type Instron machine. Shear strains were measured with the aid of a Gaertner tele–microscope. The relative displacement of adjacent sides of specimens was observed. This displacement divided by the gap of .05 in. provided the shear strain. Failed specimens are presented in Fig. 19.

Test results are presented in Table 5 and typical shear stress–shear strain curves are shown in Figs. 20 and 21. The curves exhibit a peculiar S–shape having a low initial slope followed by a sharply increased slope. The curves flatten out again for high stress levels. A possible physical explanation for this effect is as follows.

The woven fabric layers are pressed against each other. Initially the laminae are able to slip until the hills and valleys formed by the weave come in contact. When this happens the material exhibits an increased stiffness. With additional stress the laminae are again able slip past each other resulting in a lowered stiffness.

Average slopes have been used for the evaluation of G_{AW} and G_{AF}.

Table 5. Interlaminar Shear Data

Test Direction	Shear Modulus $G \times 10^4$ psi	Shear Strength $R \times 10^3$ ksi
W	$G_{CW} = 2.5$	$R_{CW} = 2.00$
F	$G_{CF} = 1.8$	$R_{CF} = 1.58$

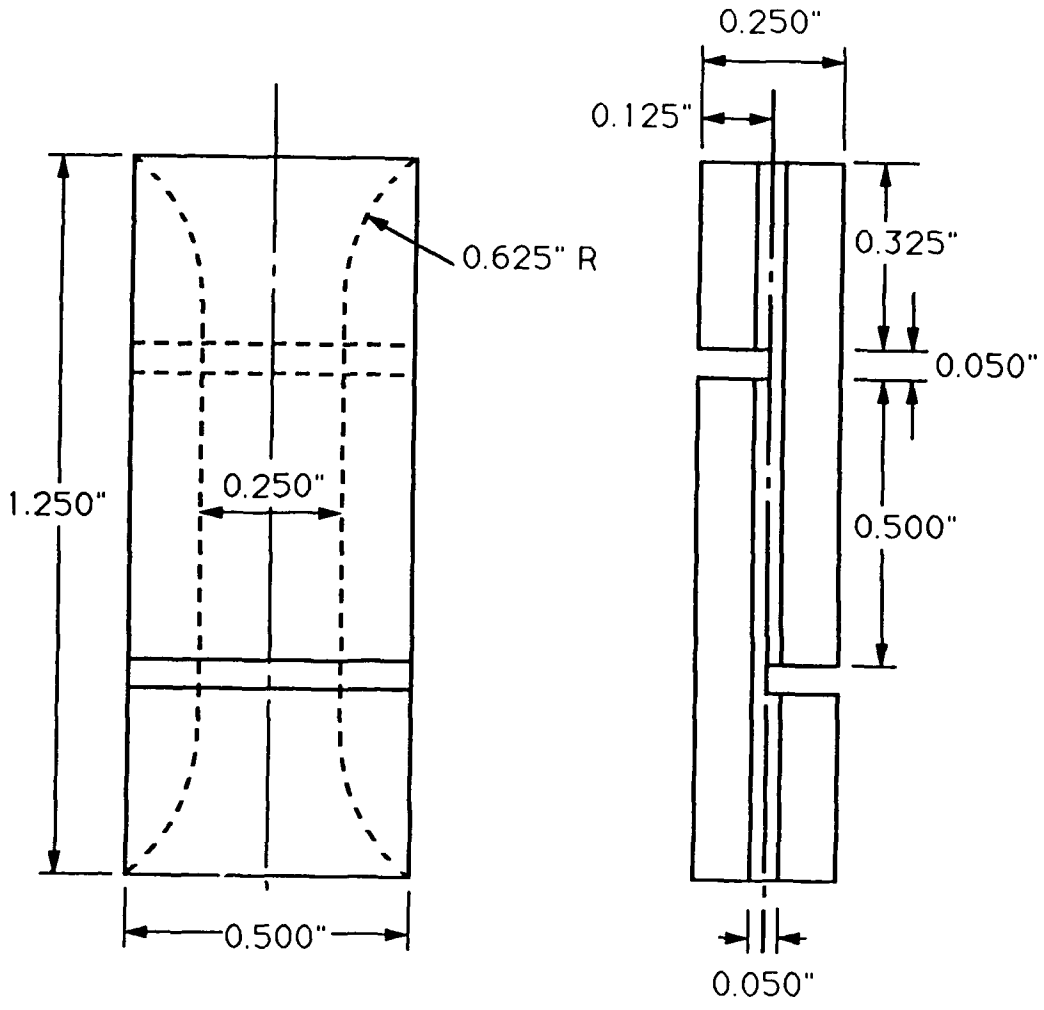

Figure 18
Dimensions of inter–laminar shear specimen

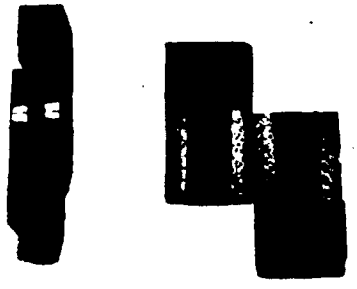

Figure 19
Failed inter–laminar shear specimens

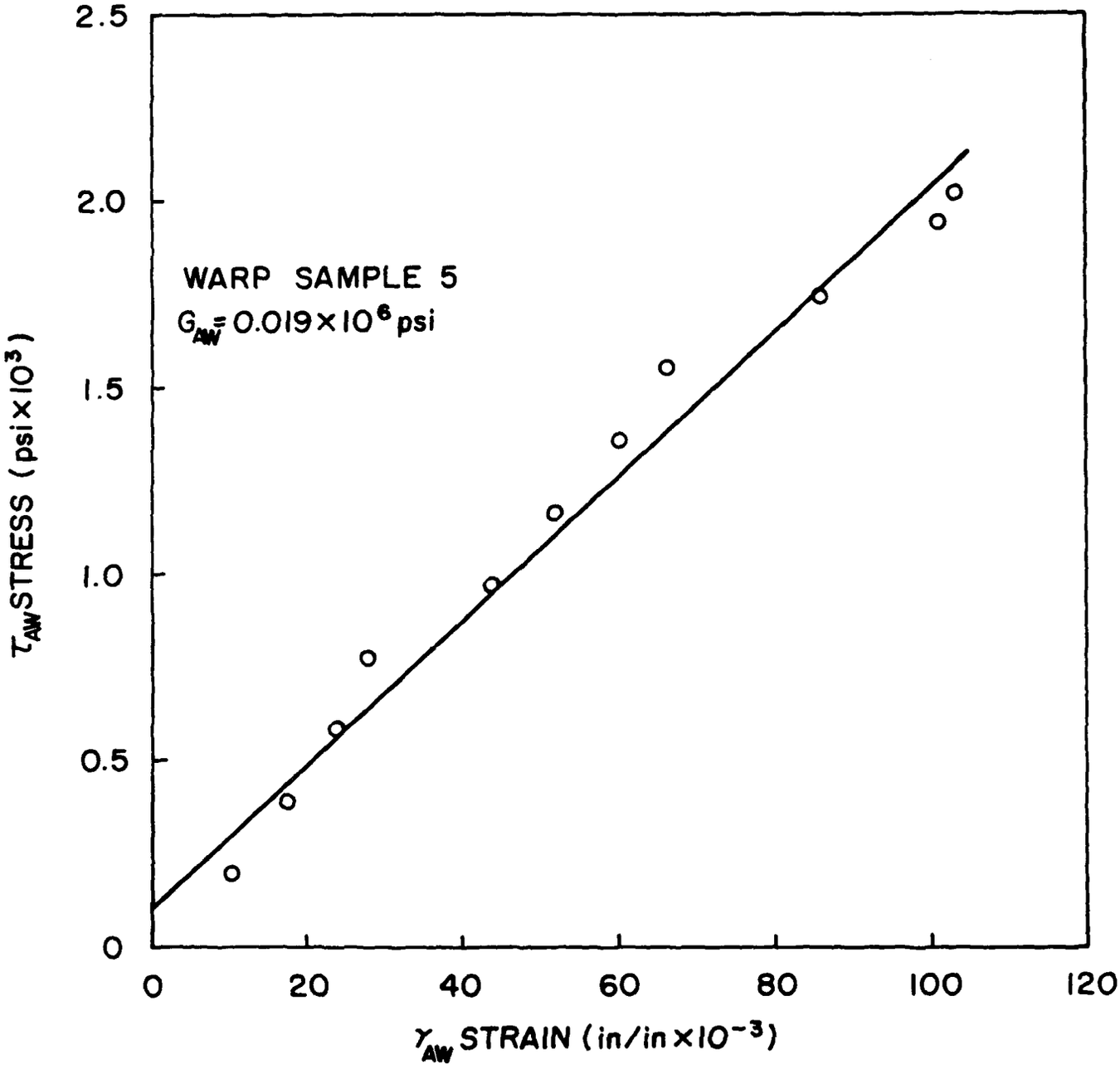

Figure 20
Inter–laminar shear stress–shear strain, R_{31}–γ_{31} curves for warp direction

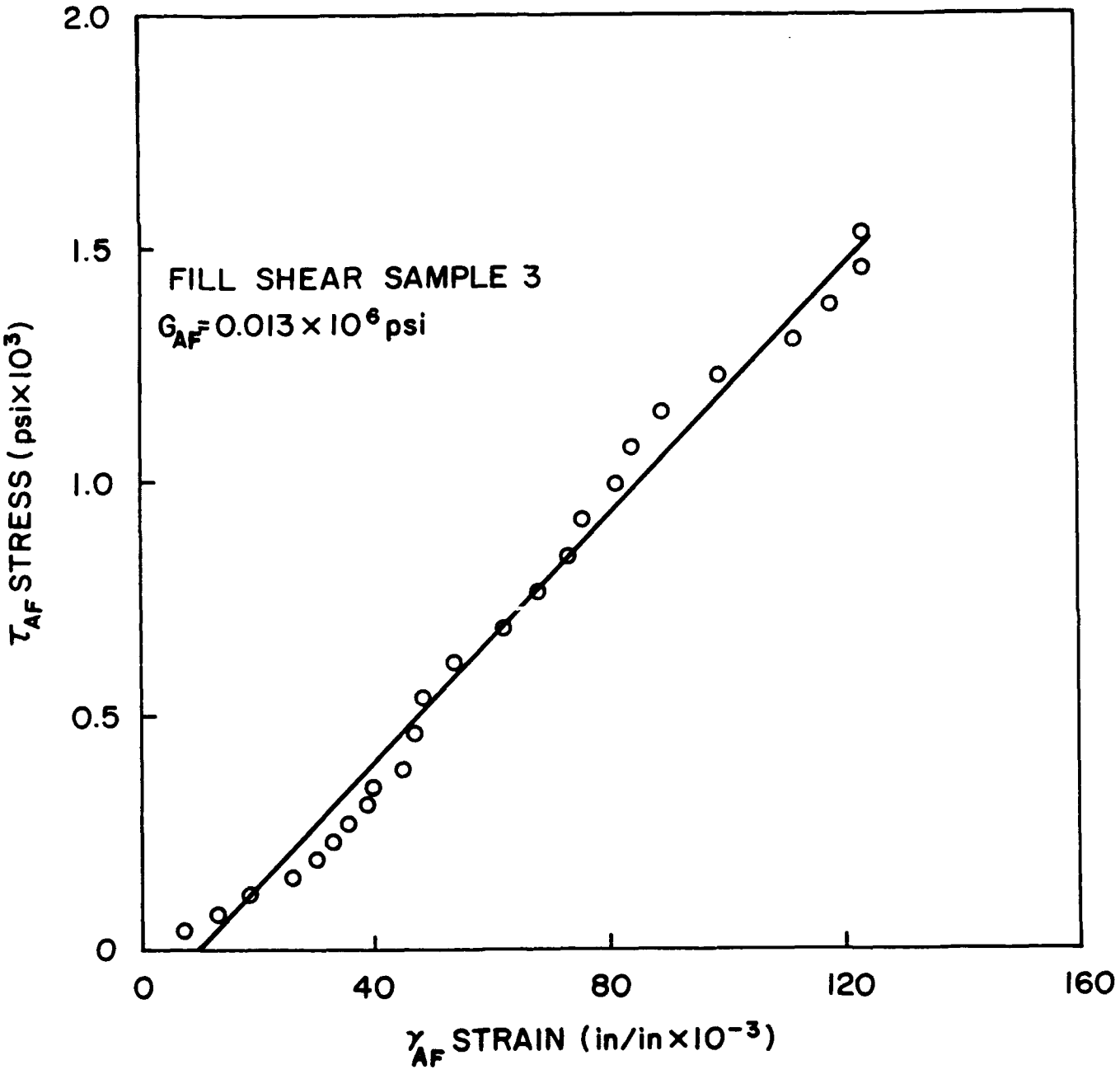

Figure 21
Interlaminar shear stress–shear strain R_{32}–γ_{32}, curves for fill direction

IN–PLANE SHEAR TESTS

To determine the shear moduli, G_{WF}, G_{FW}, G_{WC} and G_{FC} as well as the shear strengths R_{WF}, R_{FW}, R_{WA} and R_{FA}, tests were performed in a modified losipescu type fixture. Specimen dimensions are shown in Fig. 22 and failed specimens are in Fig. 23.

Test samples were cut with their longitudinal dimensions parallel to the warp (W) and fill directions (F) respectively, while their width were along each of the three directions: warp (W), fill (R) and across–ply (A).

Loads were applied in an Instron machine. Shear strains were obtained from strain gage measurements at 45° to the load direction while shear stresses were calculated as the load divided by the cross–sectional area A,

$$\gamma = 2\epsilon_{45} \tag{6}$$

and

$$\tau_{xy} = P/A \tag{7}$$

While there is some controversy about the validity of the losipescu tests, it is the only experiment that could be performed on the small specimens available.

The results are tabulated in Table 6 and typical shear stress–shear strain diagrams are plotted in Figs. 24–27.

Table 6. In–plane Shear Data

No. of specimens tested	Specimen Type	Test direction	Modulus $\bar{G}$, ksi × 10^3	σ_G, ksi × 10^3	Shear Strength $\bar{R}\times y_{max}$, ksi	σ_R, ksi	Shear Strain γ_{xymax}, in/in×10^{-3}	σ_γ in/in×10^{-3}
2	A	FA	.287	––	2.494	––	15.682	––
3	B	WA	.366	.017	3.251	.451	22.907	11.803
3	C	WF	.305	.101	4.328	.261	43.11	13.928
5	D	FW	.246	.100	3.947	.745	37.24	10.681

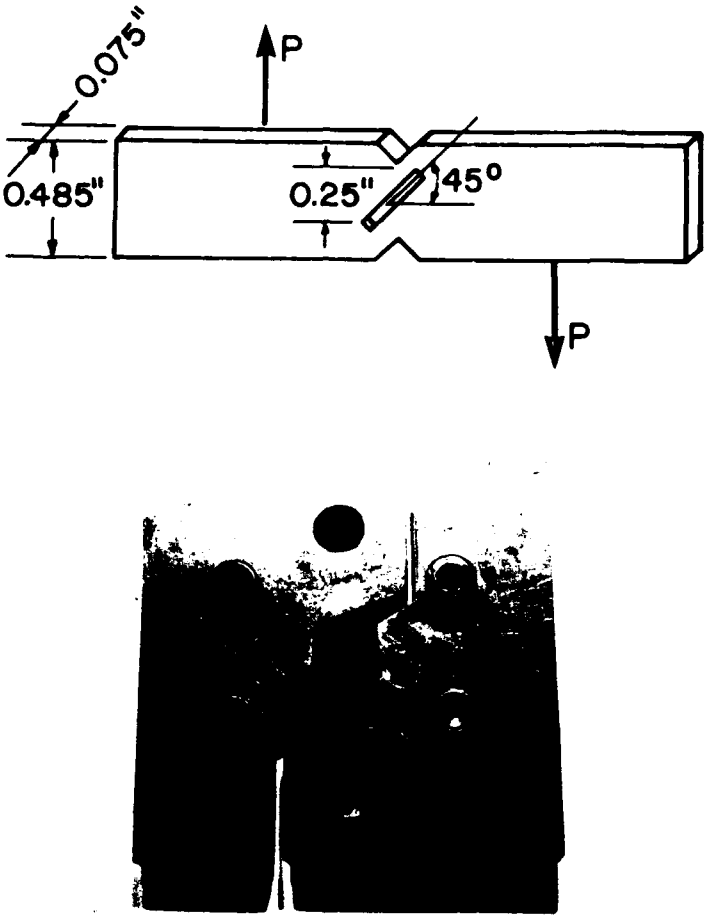

Figure 22
Iosipescu type shear specimen and test fixture.

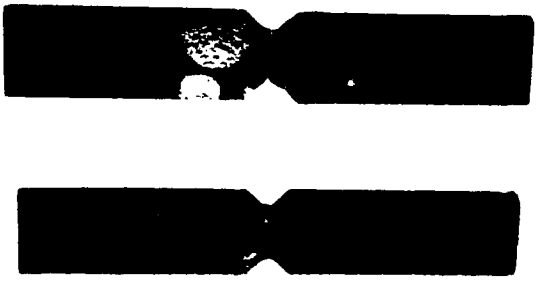

Figure 23
Failed in–plane shear specimens

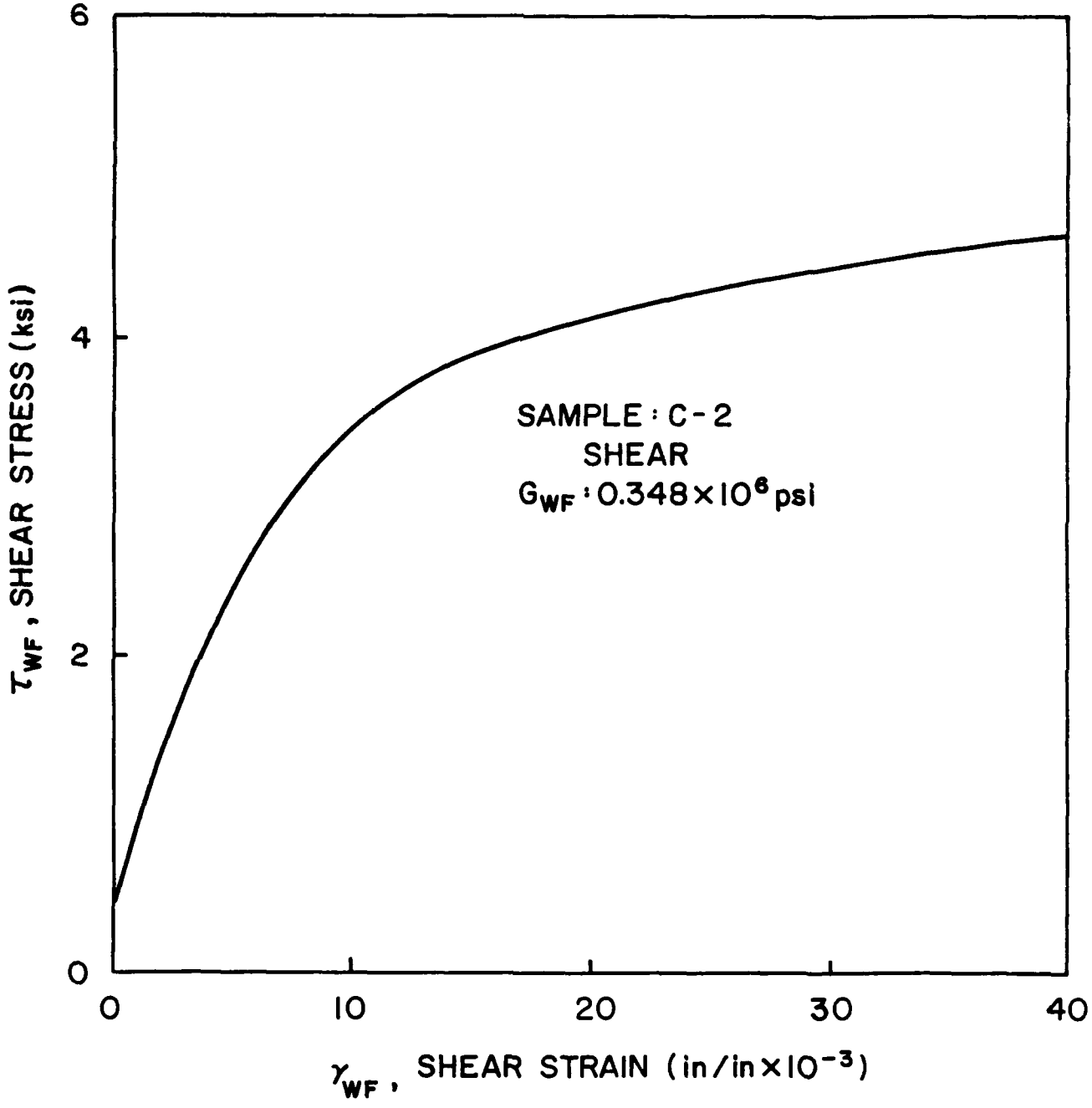

Figure 24
In–plane shear stress–shear strain, R_{WF}–γ_{WF}, curve

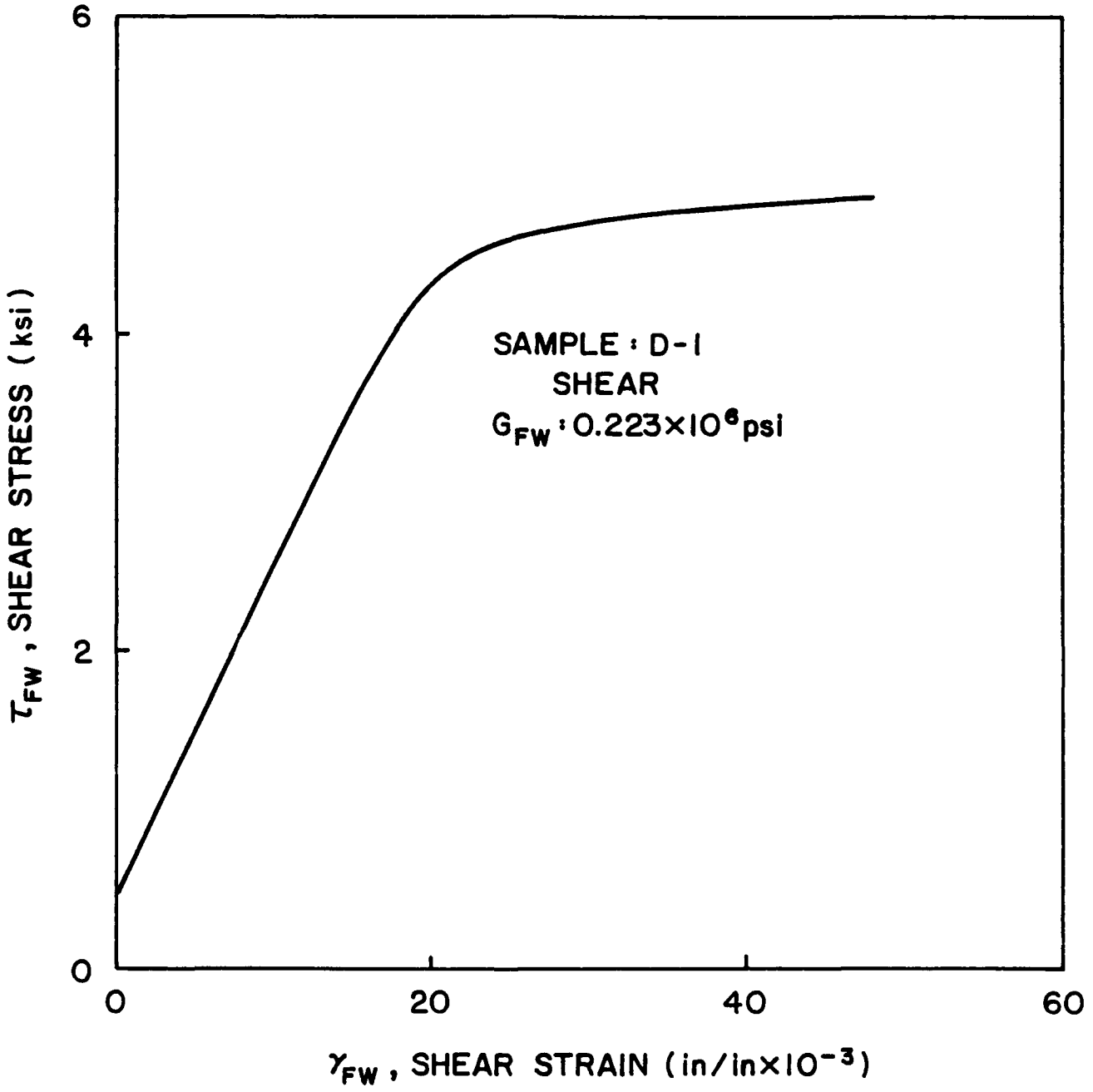

Figure 25
In–plane shear stress–shear strain, R_{FW}–γ_{FW}, curve

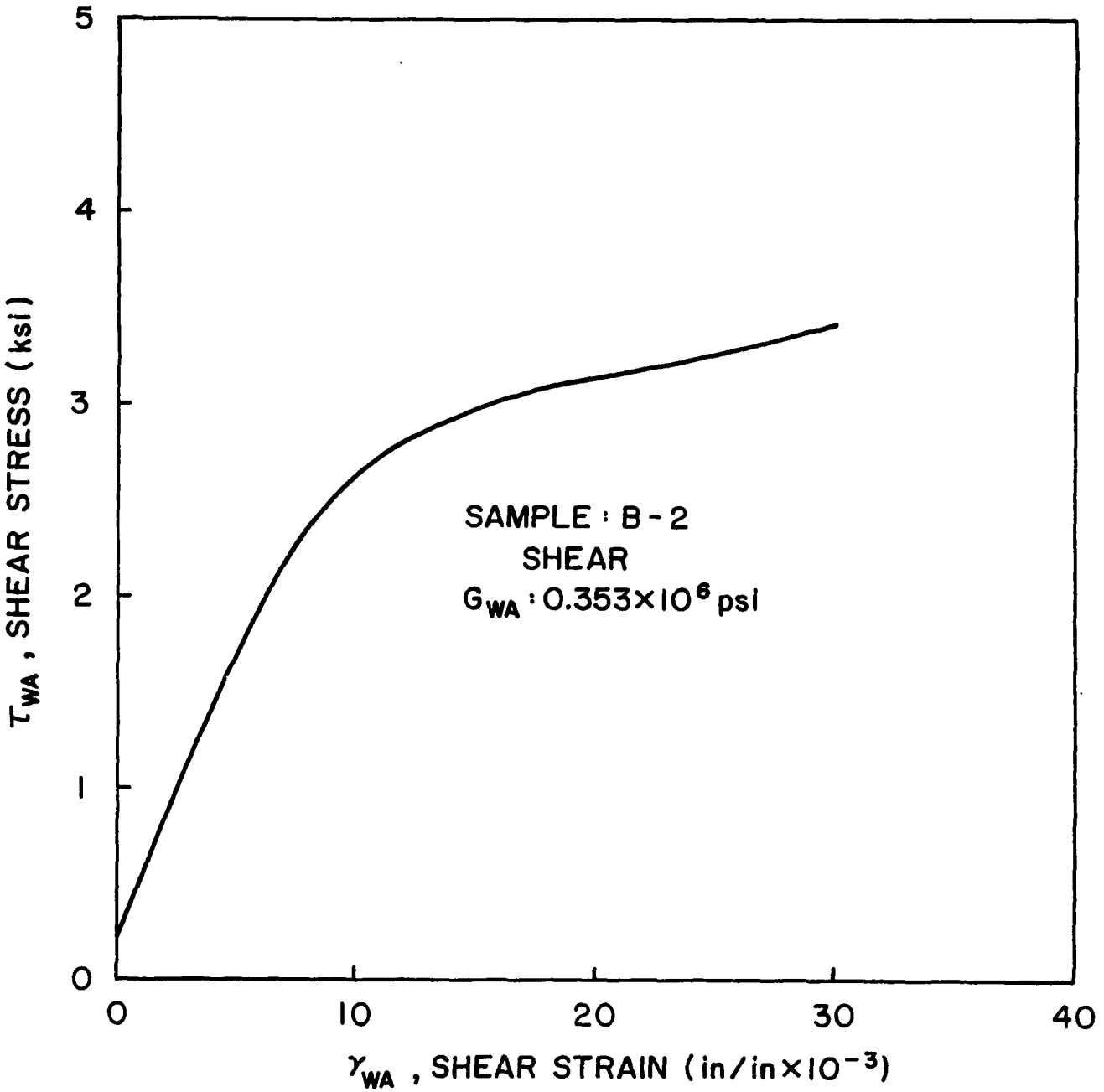

Figure 26
In–plane shear stress–shear strain R_{WA}, γ_{WA} curve

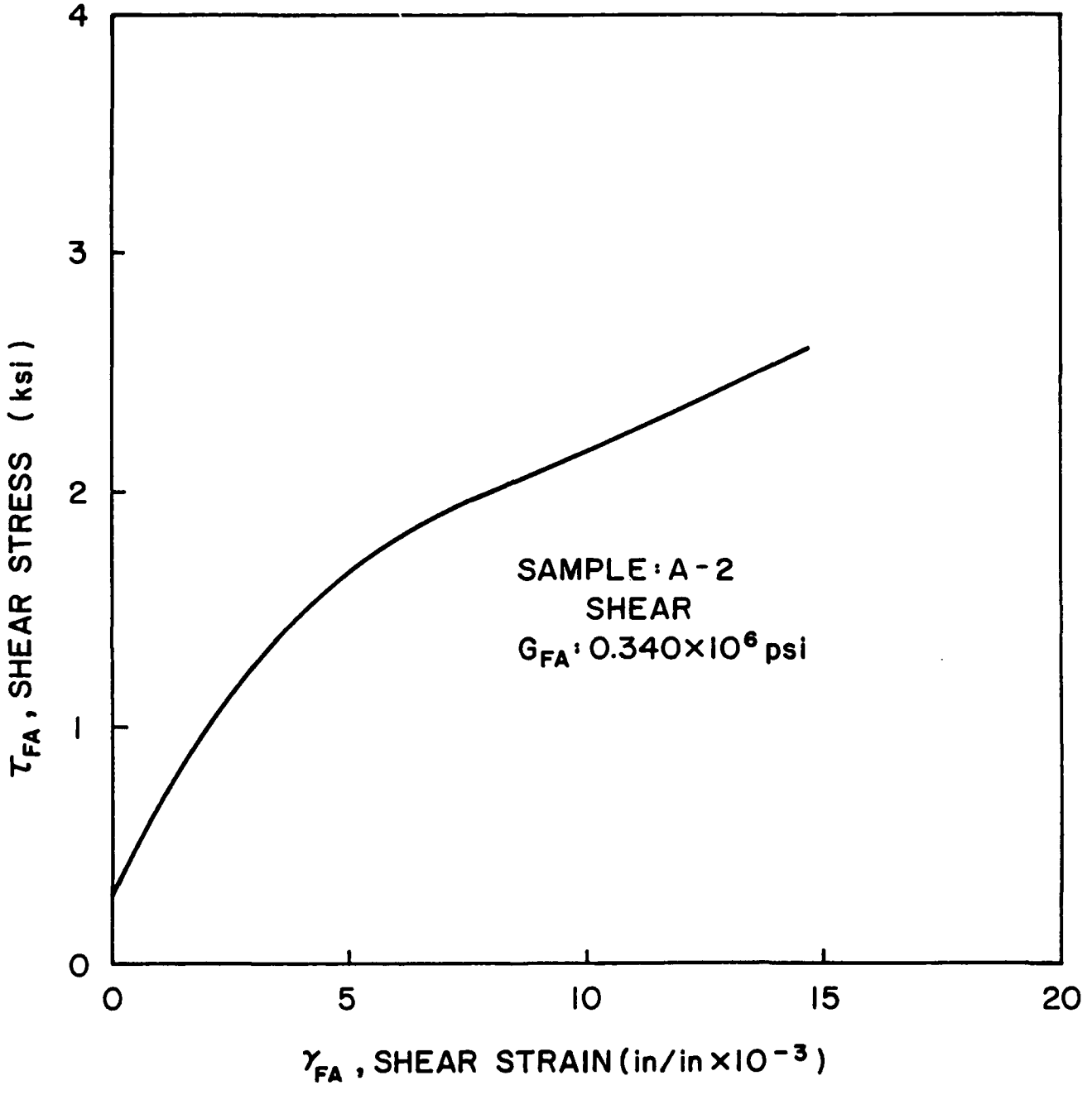

Figure 27
In–plane shear–stress–shear–strain R_{FA}–γ_{FA} curve

PROOF LOAD TESTS

The concept of proof–loading in order to increase the reliability of structures has been suggested as a promising method[5]. This technique consists of the application of a load that produces no damage in the average structure. Components that fail below the proof load are discarded while the remaining ones are assumed to have strengths greater than the stress induced by the proof load. It is, therefore, necessary to determine the level of a non–damaging proof stress that is still high enough to eliminate weak components.

Two types of tests were performed for this purpose. In one, specimens were loaded to a relatively low stress level, then unloaded and subsequently reloaded to increasingly higher levels, followed each time by unloading. This process was repeated four times. On the fifth load application, specimens were tested to failure.

The second type of test consisted of a proof stress of 80% of the average ultimate strength followed by unloading and reloading to failure. In these experiments, specimens were nondestructively tested in the DMA system before (Figs. 28 and 30) and after the application of the proof load (Figs. 29 and 31). Because the DMA machine requires very thin test samples (.05 in) such tests could not be carried out on the ordinary tension specimens used in the repeated load cycle tests.

Averaged data are presented in Tables 7 and 8 and typical stress–strain curves are plotted in Figs. 32 and 34. The results indicate a reduction in the elastic moduli in both the warp and fill directions upon reloading. While this "softening" may be considered a sign of damage, the ultimate strength of the material remained within the statistical variability of virgin specimens (Table 2).

It should be noted that in the first type of tests, the modulus was lower during the first, relatively low level load cycle. It increased in the second load cycle to a value commensurate with those of ordinary tension specimens and then decreased gradually in subsequent cycles. In the second type of test, the low modulus during proof loading was not observed.

It is assumed that initially fibers undergo a certain amount of straightening which is responsible for the low modulus values for smaller loads. This low modulus is not apparent in ordinary tension tests or in the second type of proof tests.

The tests indicate that an 80% proof stress applied to specimens produces a lowered modulus but does not degrade the ultimate strength of the material. A lower modulus will also result in decreased stresses in structural components and hence proof loading can be considered as beneficial to the reliability of structures unless the structure is designed for stiffness. None of the specimens failed during the proof cycle because the number of specimens tested was too low to observe failures.

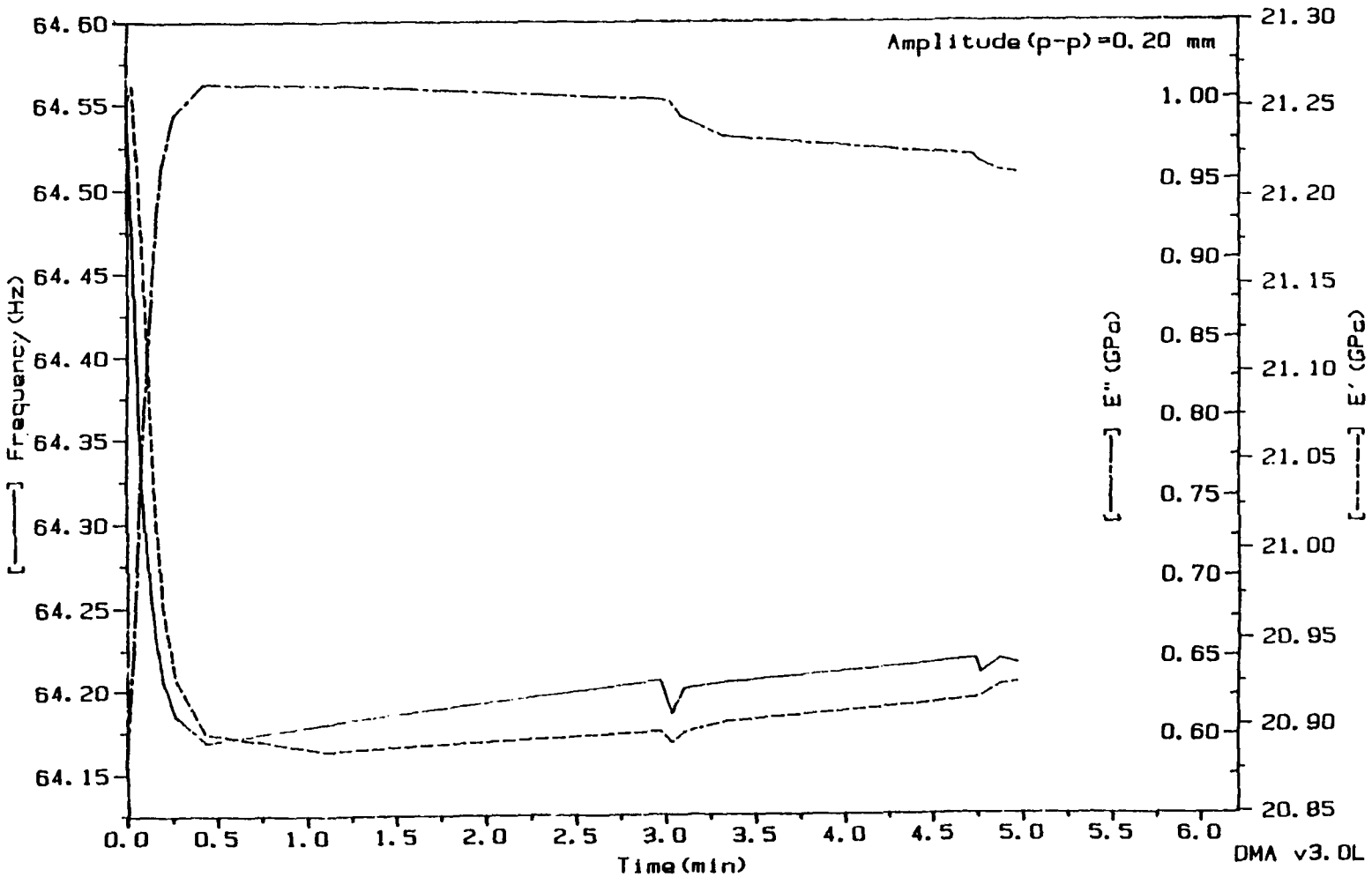

Figure 28
Plot of storage (elastic) modulus E′, loss modulus, E′′ and natural frequency before proof load. Warp specimen

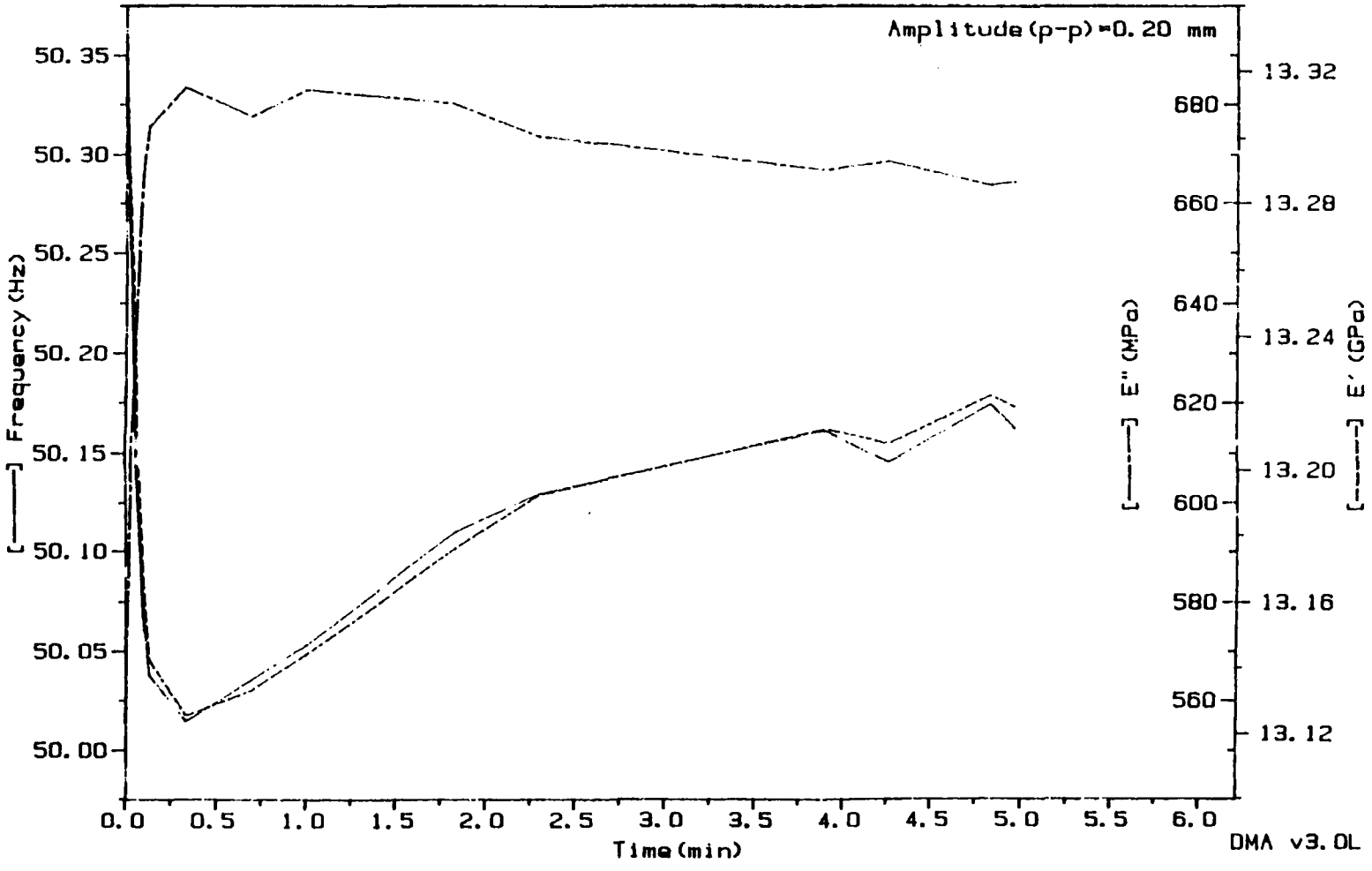

Figure 29
Plot of storage (elastic) modulus E′, loss modulus, E′′, and natural frequency after 80% proof load. Warp specimen.

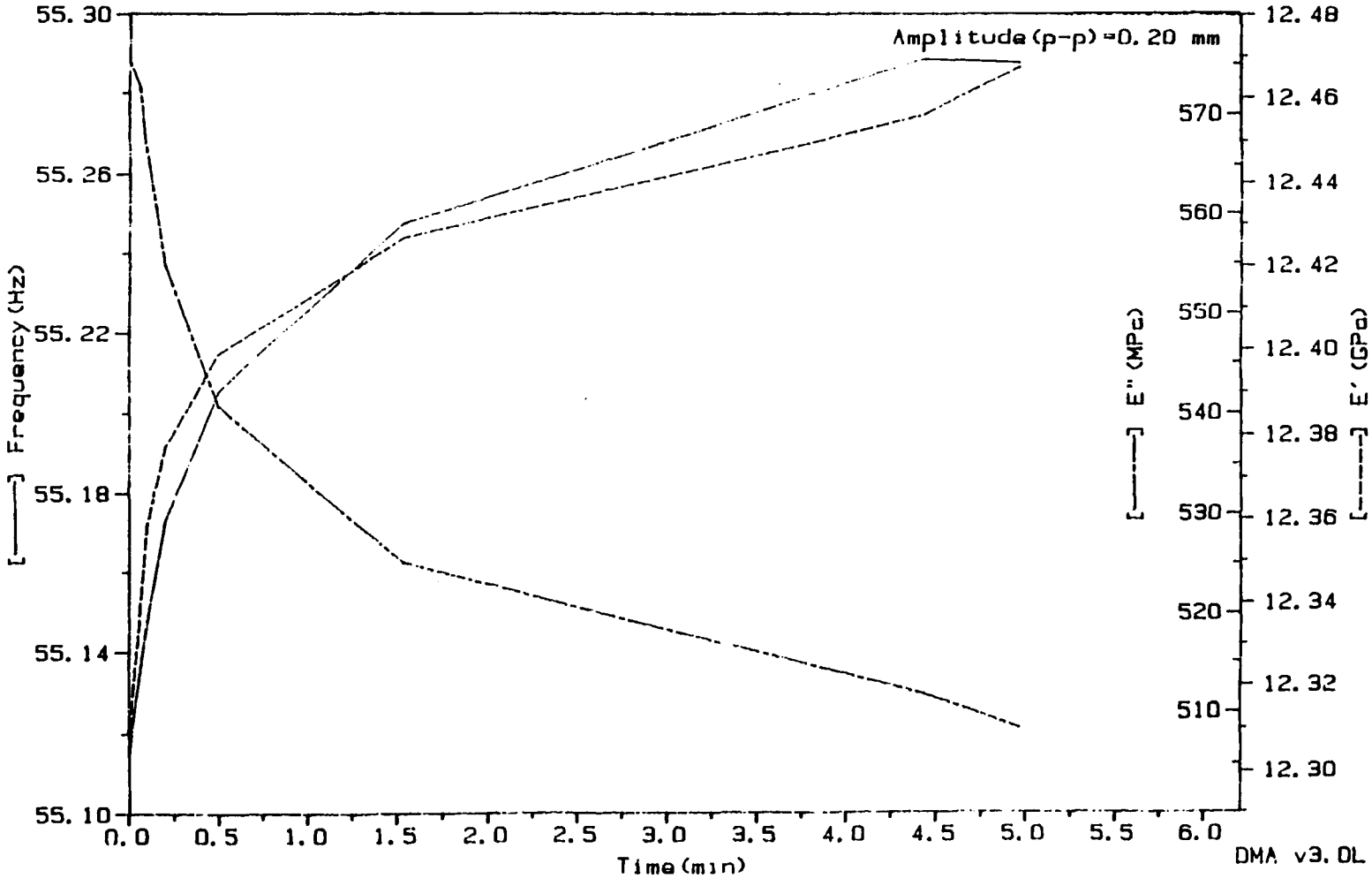

Figure 30
Plot of storage (elastic) modulus E′, loss modulus, E′′, and natural frequency before 80% proof load. Fill specimen.

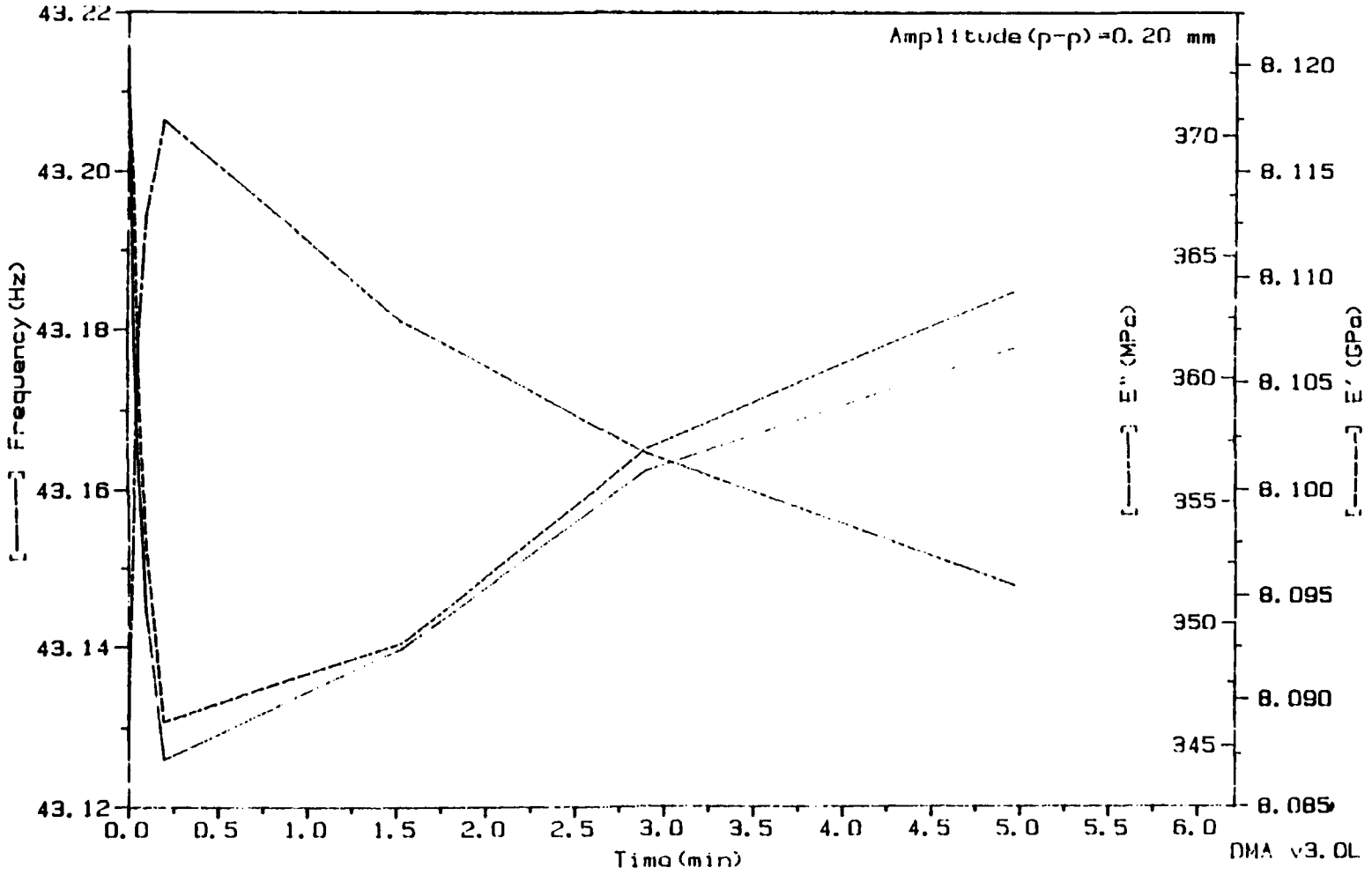

Figure 31
Plot of storage (elastic) modulus E′, loss modulus, E′′, and natural frequency after 80% proof load. Fill specimen.

Table 7. Proof–load Test Results with Repeated loads

Load Direction	Load Sequence	Modulus E×ksi×10^3	Std. Deviation (σ_E)	S_{max} ksi	Std. Deviation (σ_S)
W	1	1.811	.282		
	2	2.247	.140		
	3	2.157	.119		
	4	2.078	.135		
	5	1.993	.118	12.428	1.421
F	1	1.186	.183		
	2	1.317	.170		
	3	1.234	.166		
	4	1.144	.165		
	5	1.014	.182	5.558	20.341

Table 8. 80% Proof Load Test Results

Load Direction	Test Sequence	Modulus ksi×10^3	Stress ksi	ϵ_{max} ×10^{-3} in/in
W	DMA	2.560		
	80% Load	2.368	12.174	5.460
	Unload	2.344		
	DMA	1.679		
	Test to failure	2.389	14.710	7.100
F	DMA	1.508		
	80% Load	1.408	4.729	5.540
	Unload	0.981		
	DMA	1.294		
	Test to failure	1.032	5.517	7.276

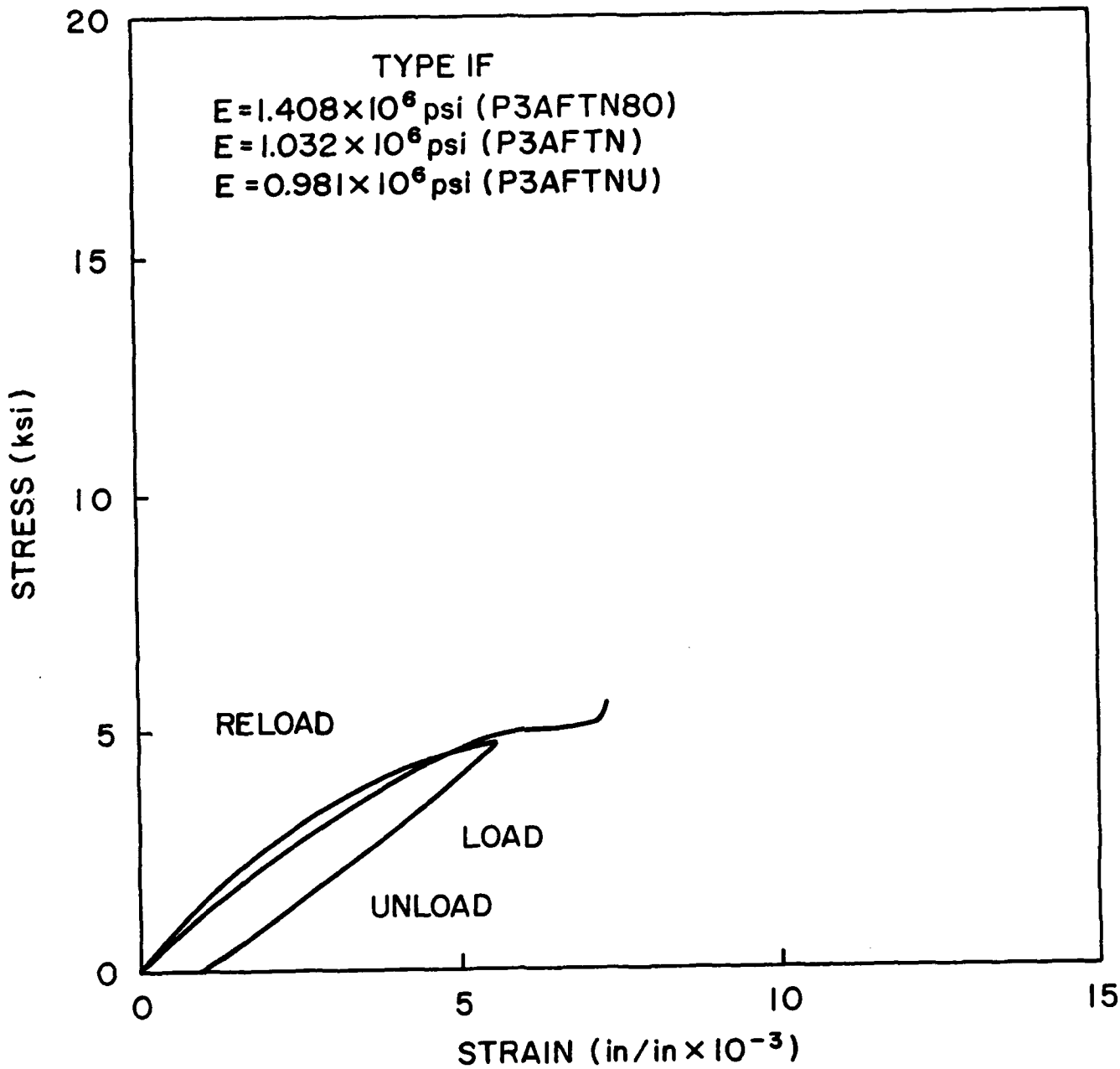

Figure 32
Stress–strain curves for proof–loaded (80%) fill specimen.

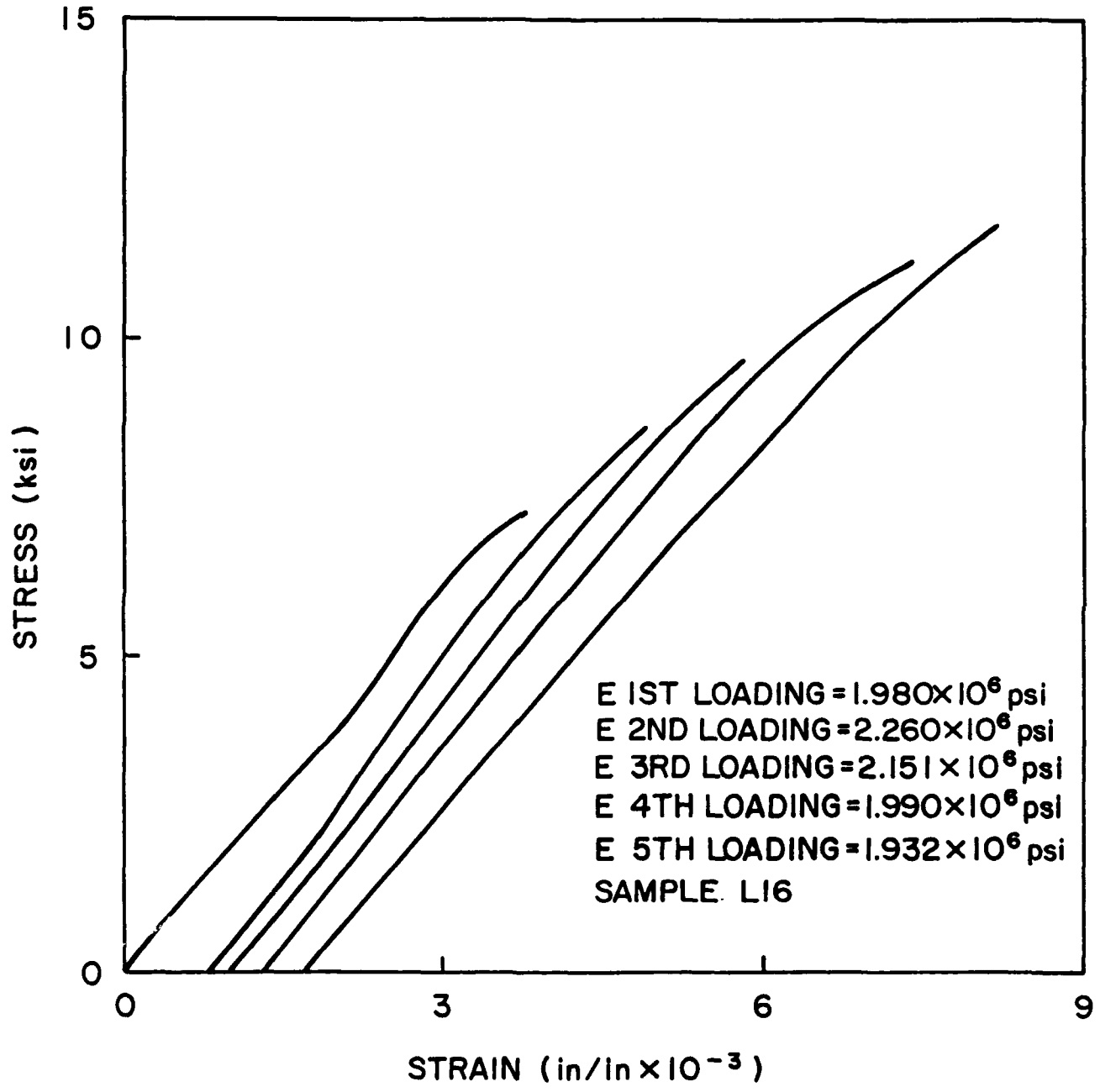

Figure 33
Stress–strain curves for repeated loads (warp specimen).

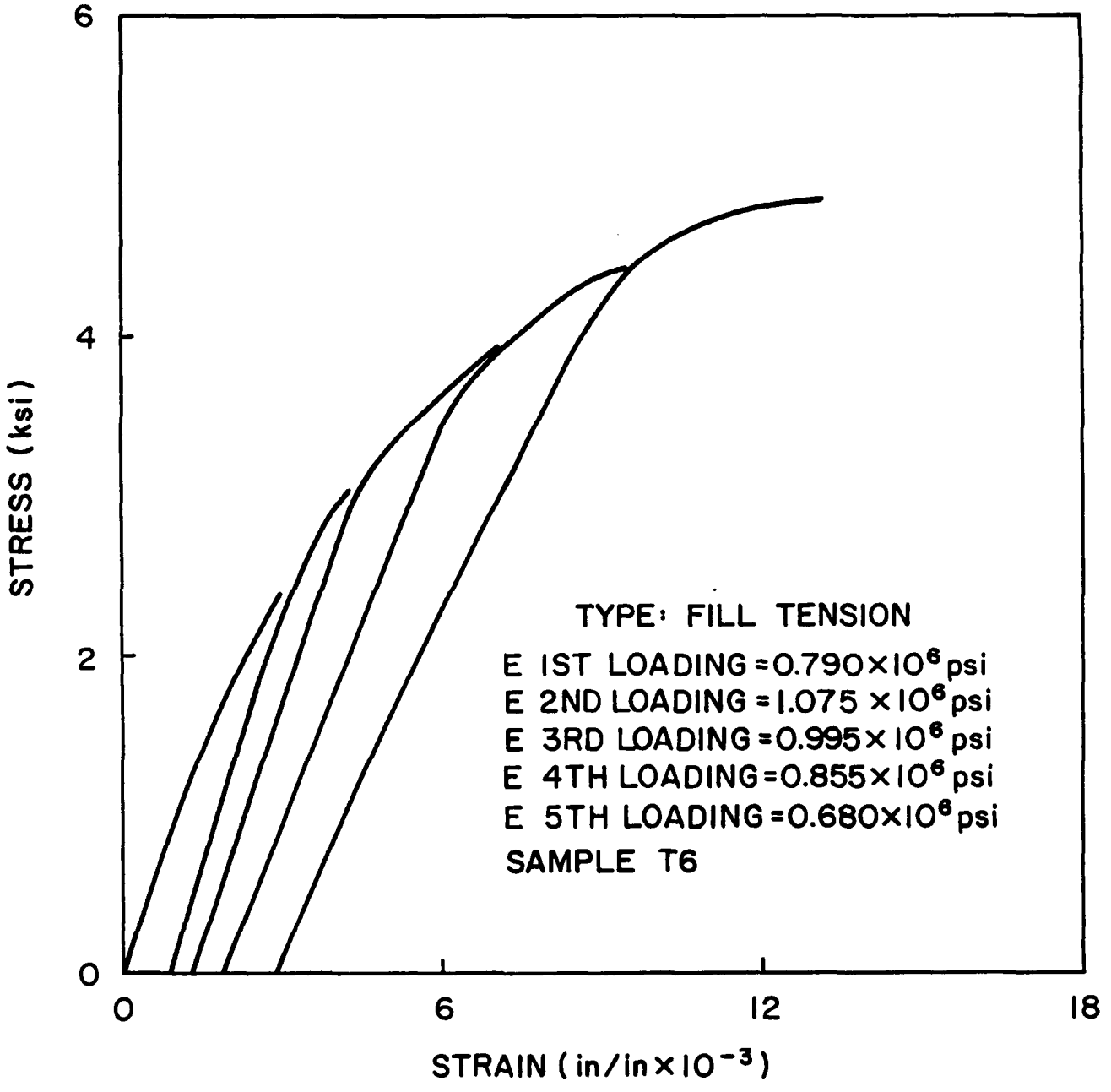

Figure 34
Stress–strain curves for repeated loads (fill specimen).

WEIBULL DISTRIBUTION PARAMETERS

One of the aims of the experimental investigations presented here is the determination of the statistical distributions that will best describe the dispersion of mechanical properties.

A three parameter Weibull distribution has been fitted to the tension strength data. Warp and fill results were combined in order to increase the size of the population. This was accomplished by the introduction of a normalized variable, $r = R/\bar{R}$ where R is the strength of a sample and $\bar{R}$ is the mean strength in the appropriate direction.

For the three parameter Weibull reliability function,the probability of exceedence, $L_r(r)$ is written as

$$L_r(r) = e^{-\left[\frac{r-r_o}{r_c-r_c}\right]^m} \tag{8}$$

where r_o is the normalized minimum strength below which no failure is expected, r_c is the characteristic value with a probability of exceedence of $L_{(r_c)} = e^{-1}$, and m is the shape parameter which is a measure of dispersion.

The relationships between mean, standard deviation, characteristic value and shape parameters are transcendental equations

$$\bar{r} = (r_c - r_o)\Gamma(1 + \frac{1}{m}) + r_o \text{ and} \tag{9}$$

$$\sigma_r^2 = (r_c - r_o)\left[\Gamma(1 + \frac{2}{m}) - \Gamma^2(1 + \frac{1}{m}\right]^{\frac{1}{2}} \tag{10}$$

where $\Gamma(\cdot)$ is the tabulated gamma function. The following parameters were calculated

$$m = 6.17$$
$$r_o = 0.61$$
$$r_c = 1.03$$

From these, the distribution parameters for the warp and fill directions become

Warp	Fill
$m = 6.17$	$m = 6.17$
$R_{ow} = 8{,}110$ psi	$R_{oF} = 3440$ psi
$R_{cw} = 13{,}820$ psi	$R_{cF} = 5800$ psi

The combined data are listed in Table 9 and are plotted in Figs. 35 and 36.

These parameters will be utilized in calculations of structural reliability in conjunction with the "weakest link" principle and finite element stress analyses in Part 2 of this report.

Table 9. Normalized Tension Strength Data and Three Weibull Parameters (m = 56)

Rank i	Data r_i	$L=1-(\frac{i}{n+1})$ Reliability L_i	Rank i	Data r_i	L Reliability L_i
1	0.7699	0.9825	29	1.0048	0.4912
2	0.8126	0.9649	30	1.0063	0.4737
3	0.8915	0.9474	31	1.0140	0.4561
4	0.9091	0.9298	32	1.0143	0.4386
5	0.9186	0.9123	33	1.0166	0.4211
6	0.9319	0.8947	34	1.0184	0.4035
7	0.9330	0.8772	35	1.0211	0.3860
8	0.9330	0.8596	36	1.0225	0.3684
9	0.9330	0.8421	37	1.0280	0.3509
10	0.9377	0.8246	38	1.0287	0.3333
11	0.9379	0.8070	39	1.0327	0.3158
12	0.9396	0.7895	40	1.0336	0.2982
13	0.9425	0.7719	41	1.0373	0.2807
14	0.9435	0.7544	42	1.0478	0.2632
15	0.9455	0.7368	43	1.0478	0.2456
16	0.9494	0.7193	44	1.0524	0.2281
17	0.9572	0.7018	45	1.0526	0.2015
18	0.9657	0.6842	46	1.0585	0.1930
19	0.9669	0.6667	47	1.0670	0.1754
20	0.9762	0.6491	48	1.0717	0.1079
21	0.9803	0.6316	49	1.0717	0.1404
22	0.9814	0.6140	50	1.0861	0.1228
23	0.9850	0.5965	51	1.1002	0.1053
24	0.9856	0.5789	52	1.1040	0.0877
25	0.9925	0.5614	53	1.1042	0.0702
26	0.9980	0.5439	54	1.1203	0.0526
27	0.9998	0.5263	55	1.1508	0.0351
28	1.0048	0.5088	56	1.1646	0.0175

Shape parameter, $m = 6.17$
Characteristic value, $r_c = 1.03$
Minimum value, $r_o = 0.61$

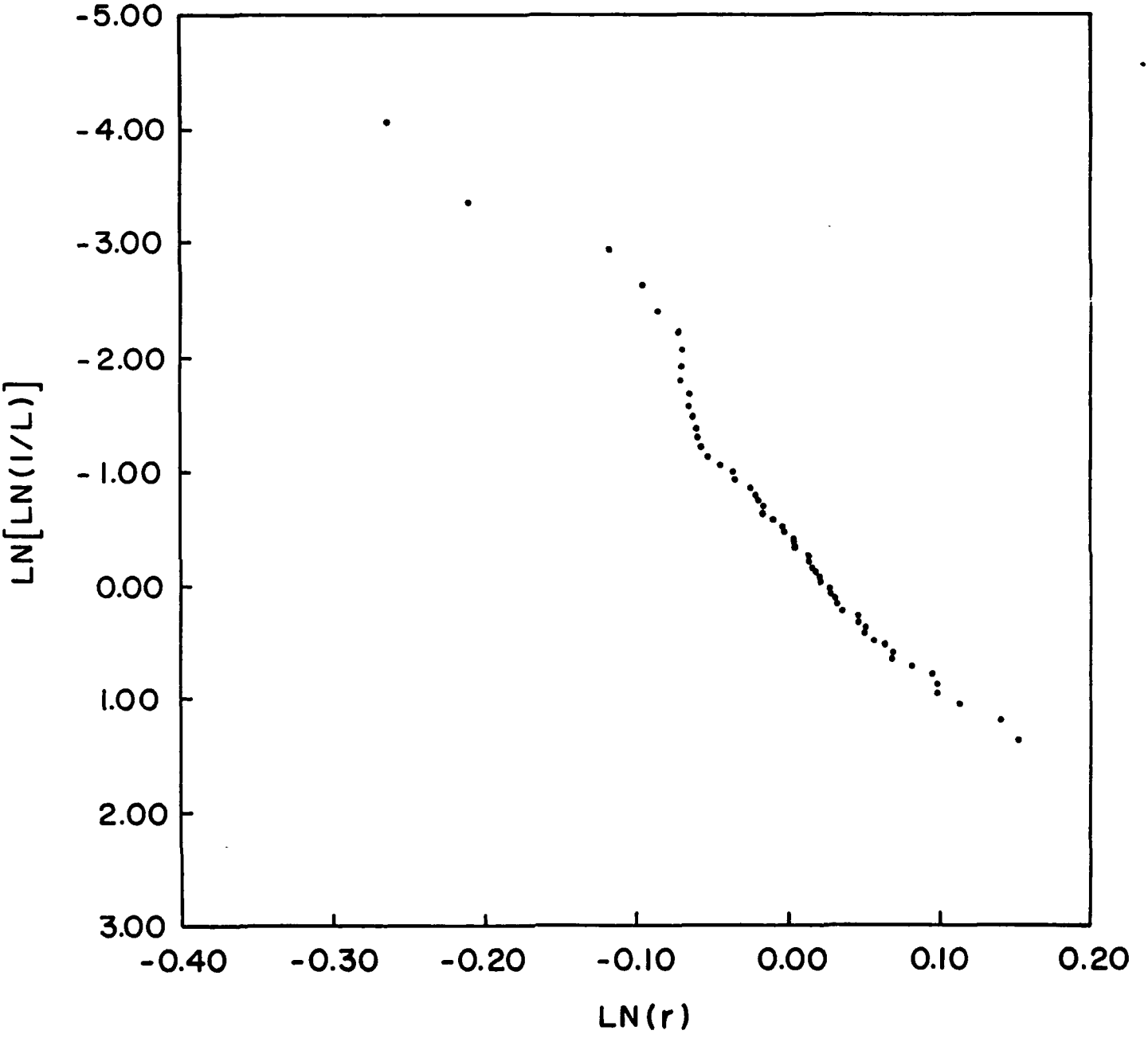

Figuer 35
Probability of exceedence in [ℓn 1/L] (reliability), versus dimensionless strength, ℓn(r), on Weibull paper.

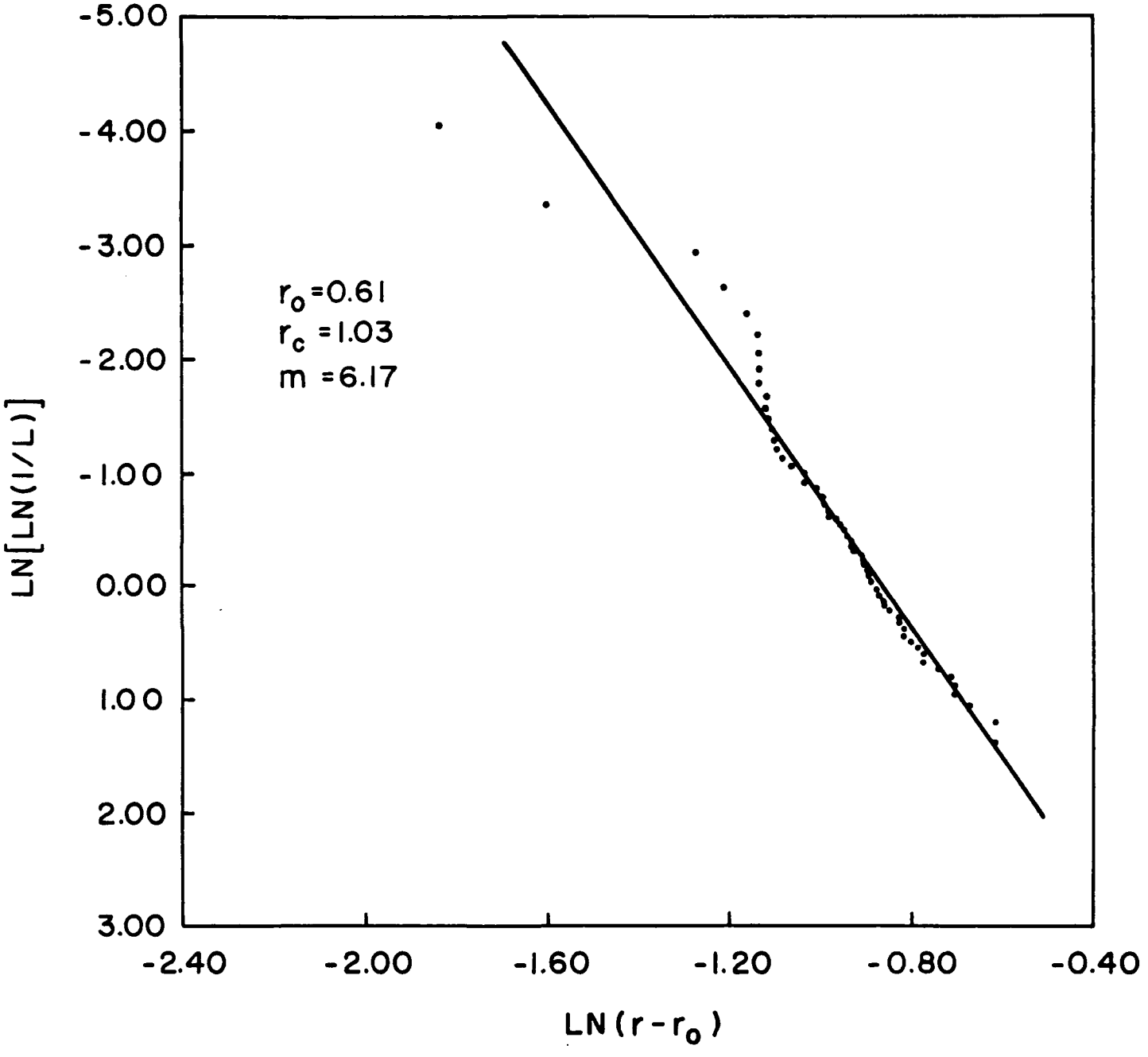

Figure 36
Probability of exceedence, ℓn [ℓn 1/L] versus $\ell n(r-r_o)$ on Weibull paper.

ORTHOTROPIC MECHANICAL PARAMETERS

It has been mentioned in Section 2 that the carbon/carbon material is modelled as a laminate consisting of alternating laminae of orthotropic fiber layers and isotropic matrix layers. The mechanical parameters: moduli and strengths, are evaluated from the previously discussed test results and where direct experimental data was not generated, from information published in Refs. 1, 2 and 6–8.

Designating the warp direction for the orthotropic fiber layer as 1, the fill direction as 2, and the cross–ply direction as 3, utilizing the experimental results of Table 2 and Eqs. 2.1 and 2.2, the following values are obtained for tension

$$E_w = v_{f1}E_{f1} + v_{m1}E_m \tag{11}$$

$$E_F = v_{f2}E_{f2} + v_{m2}E_m \tag{12}$$

with

$E_W = 2.14 \times 10^6$ psi, $E_F = 1.19 \times 10^6$ psi, $E_m = .5 \times 10^6$ psi, $v_{f1} = \frac{1}{2}$, $v_{m1} = \frac{1}{2}$, $v_{f2} = \frac{1}{3}$ $v_{m2} = \frac{2}{3}$ result in

$$E_{f1} = 3.78 \times 10^6 \text{ psi and } E_{f2} = 2.79 \times 10^6 \text{ psi}$$

Replacing the modulus terms in Eqs. 2.1 and 2.2 by strength terms and using the values of Table 2,

$$R_w = v_{f1}R_{f1} + v_{m1}R_m \tag{13}$$

$$R_F = v_{f2}R_{f2} + v_{m2}R_m \tag{14}$$

with $R_w = 13{,}400$ psi, $R_F = 5{,}600$ psi and $R_m = 2000$ psi.

$$R_{f1} = 24{,}800 \text{ psi and } R_{f2} = 12{,}000 \text{ psi},$$

are obtained for the average orthotropic strength of the fiber layer. Similar calculations based on the data of Table 2 yield the following results for compressive mechanical parameters

$$E_{f1} = 3.7 \times 10^6 \text{ psi} \qquad E_{f2} = 3.5 \times 10^6 \text{psi}$$
$$R_{fw} = 14{,}600 \text{ psi} \qquad R_{f2} = 13{,}000 \text{ psi}$$

It is assumed that the matrix material is essentially isotropic. With a modulus of $E_m = 0.5\times10^6$ psi and Poisson's ratio of 0.25, the shear modulus is estimated as

$$G_{m1} = \frac{E_m}{2(1+\nu_m)} = 0.2\times10^6 \text{ psi}$$

Utilizing this value and the test results of $G_{WF} = 0.355\times10^6$ psi, $G_{FW} = 0.246\times10^6$ psi together with the volume fractions $v_{f1} = 1/2$, $v_{m1} = 1/2$, $v_{f2} = \frac{1}{3}$ and $v_{m2} = \frac{2}{3}$ in the equations

$$G_{WF} = v_{f2}G_{f12} + v_{m2}\times(0.2\times10^6) \quad (15)$$

$$G_{FW} = v_{f1}G_{f21} + v_{m1}\times(0.2\times10^6) \quad (16)$$

the following fiber layer shear moduli are obtained:

$$G_{f12} = .67\times10^6 \text{ psi}, \; G_{f21} = .29\times10^6 \text{ psi}$$

Similarly the fiber layer shear strengths are calculated as

$$R_{f12} = 9900 \text{ psi and } R_{f21} = 6500 \text{ psi}$$

from the tabulated test results: $R_{WF} = 4300$ psi, $R_{FW} = 4000$ psi and an $R_{sm} = 1500$ psi estimated from the results of interlaminar shear tests, Section 7.

It should be recognized that across–ply parameters measured for the laminate can not be separated into fiber and matrix layer values.

The calculated and/or assumed parameters are summarized in Table 10.

Table 10. Average Mechanical Parameters

(W = 1 = warp, F = 2 = fill, A = 3 = across–ply directions, f = fiber, m = matrix)

	Composite	Fiber Layer
	Modulus × 10^6 psi	Modulus × 10^6 psi
Tension	$E_W = 2.140$	$E_{f1} = 3.780$
	$E_F = 1.190$	$E_{f2} = 2.790$
	$^{**}E_A = .855$	$^{**}E_3 = .855$
	$^{*}E_m = 0.500$	$^{*}E_m = 0.500$
Compression	$E_W = 2.130$	$E_{f1} = 3.700$
	$E_F = 1.500$	$E_{f2} = 3.500$
	$^{**}E_A = .820$	$^{**}E_3 = .820$
	$^{*}E_m = 0.500$	$^{*}E_m = 0.500$

Table 10. *Continued*

	Composite	Fiber Layer
Shear	$G_{WF} = 0.355$ $G_{FW} = 0.246$ $G_{WA} = 0.357$ $G_{FA} = 0.340$ $G_{FW} = 0.025$ $G_{AF} = 0.018$ $*G_{sm} = 0.200$	$G_{12} = 0.670$ $G_{21} = 0.290$ $G_{13} = 0.357$ $G_{23} = 0.340$ $G_{31} = 0.025$ $G_{32} = 0.013$ $*G_{sm} = 0.200$
	Strength psi	Strength psi
Tension	$R_W = 13{,}400$ $R_F = 5600$ $**R_A = 8800$ $*R_m = 2000$	$R_{f1} = 24{,}800$ $R_{f2} = 12{,}000$ $**R_3 = 8800$ $*R_m = 2000$
Compression	$R_W = 8300$ $R_F = 5700$ $**R_A = 24{,}000$ $*R_m = 2000$	$R_{f1} = 14{,}000$ $R_{f2} = 13{,}000$ $**R_3 = 24{,}000$ $*R_m = 2000$
Shear	$R_{WF} = 4300$ $R_{FW} = 4000$ $R_{WA} = 4000$ $R_{FA} = 4100$ $R_{AW} = 2000$ $R_{AF} = 1600$ $*R_{sm} = 1500$	$R_{f12} = 9900$ $R_{21} = 6{,}400$ $R_{13} = 4000$ $R_{23} = 4100$ $R_{31} = 2000$ $R_{32} = 1600$ $*R_{sm} = 1500$

Table 10. Continued

Composite	Fiber Layer
Poisson's ratio	Volume fraction
$\nu_{12} = .048$	$v_{f1} = .500$
$\nu_{21} = .093$	$v_{m1} = .500$
$^{**}\nu_{21} = .200$	$v_{f2} = .333$
$\nu_{31} = .426$	$v_{m2} = .667$
$\nu_{32} = .203$	
$^{**}\nu_{23} = .210$	
$\nu_m = .250$	

* Estimated values
** From Ref. 1

BENDING TESTS ON NOTCHED AND UN–NOTCHED BEAMS

To demonstrate the presence of size effects in carbon/carbon it would be necessary to test specimens with widely differeing volumes. Based on the "weakest link" theory and the Weibull distribution (detailed in part two of this report) the reliability, L, of a specimen subjected to uniform tension stress is

$$L = e^{-\left[\frac{R-R_o}{R_c-R_o}\right]^m \frac{V}{V_r}} \tag{17}$$

where R is the strength of the specimen of volume V, R_c and R_o are the characteristic strength and the minimum strength of the reference volume, V_r.

If two specimens with different volumes are compared at the same level of reliability the exponents of Eq. 11.1 must be equated to each other.

$$\left[\frac{R_r-R_o}{R_c-R_o}\right]^m \frac{V_r}{V_r} = \left[\frac{R-R_o}{R_c-R_o}\right]^m \frac{V}{V_r} \tag{18}$$

Hence, the strength of volume V becomes

$$R = (R_r-R_o)\left[\frac{V_r}{V}\right]^{1/m} + R_o \tag{19}$$

Utilizing dimensionless variables

$r = \frac{R}{\bar{R}_r}\frac{R}{R_r}$, $r_R = 1$, $r_o = \frac{R}{\bar{R}_r}\frac{R_o}{R_r}$ and the values of the Weibull parameters listed in Table 9

$$r = (1-0.61)\left[\frac{V_r}{V}\right]^{1/6.17} + 0.61\,, \tag{20}$$

the following strength values are obtained

$\frac{V_r}{V}$	r	$\frac{V_r}{V}$	r
10000	2.34	1	1.00
1000	1.80	.1	0.88
100	1.43	.01	0.79
10	1.18	.001	0.74
3	1.08	.0001	0.70

It is seen consequently that very large volume ratios would have to be tested to observe a significant strength reduction due to the size effect. To avoid this problem, specimens with severe stress gradients such as notched beams and plates with holes are tested. As shown in part two of this report, the small, highly stressed regions in the vicinity of such stress raisers can be considered to be small volumes with increased strengths. Hence, to verify this concept, three and four point bending tests have been carried out on carbon/carbon beams. Specimens were prepared with their longitudinal axes along the warp and fill directions, respectively, as shown in Fig. 37. In each case, beams were tested as laminated composites (Type I) with loads applied perpendicularly to the laminae and, in order to avoid interlaminar shear stresses, as pseudo isotropic beams (Type 2) with loads parallel to the layers. Beam dimensions and the test configuration are presented in Fig. 38.

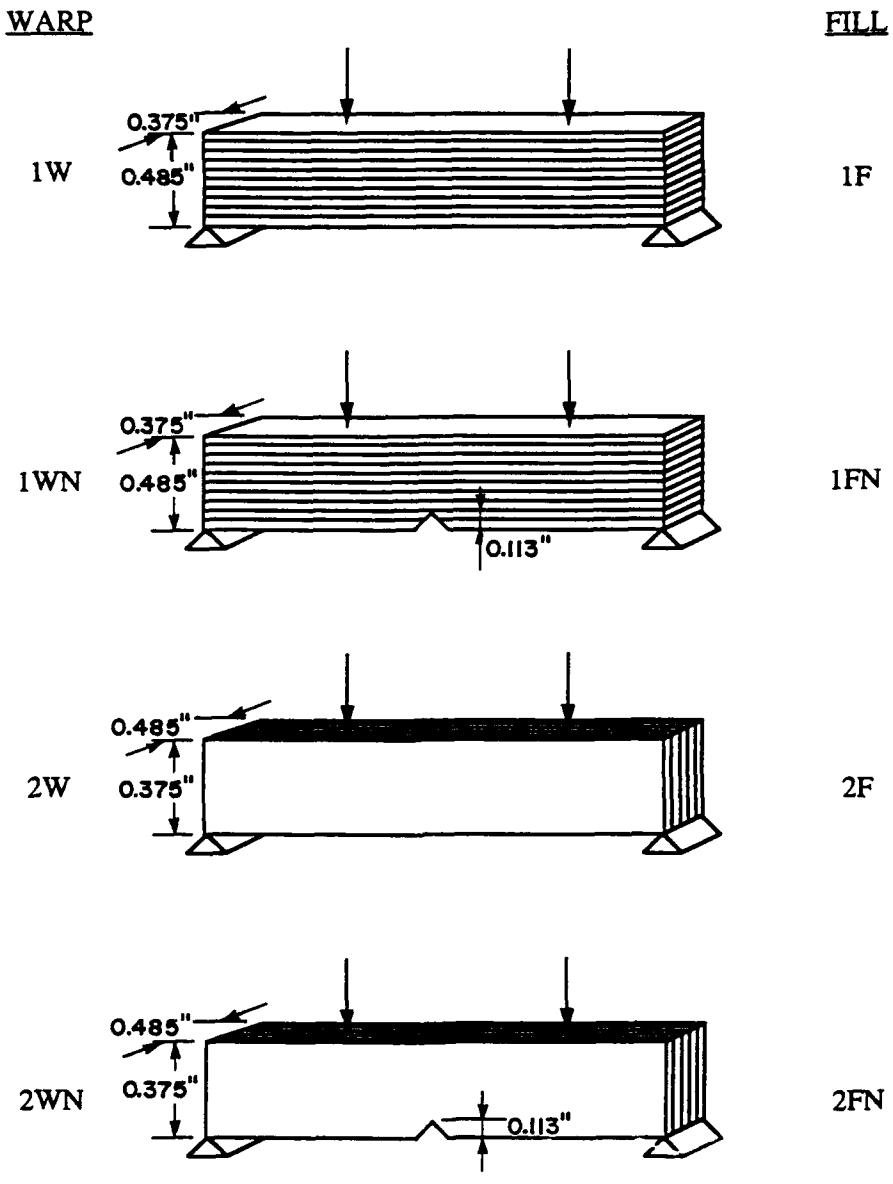

Figure 37
Bending specimens.

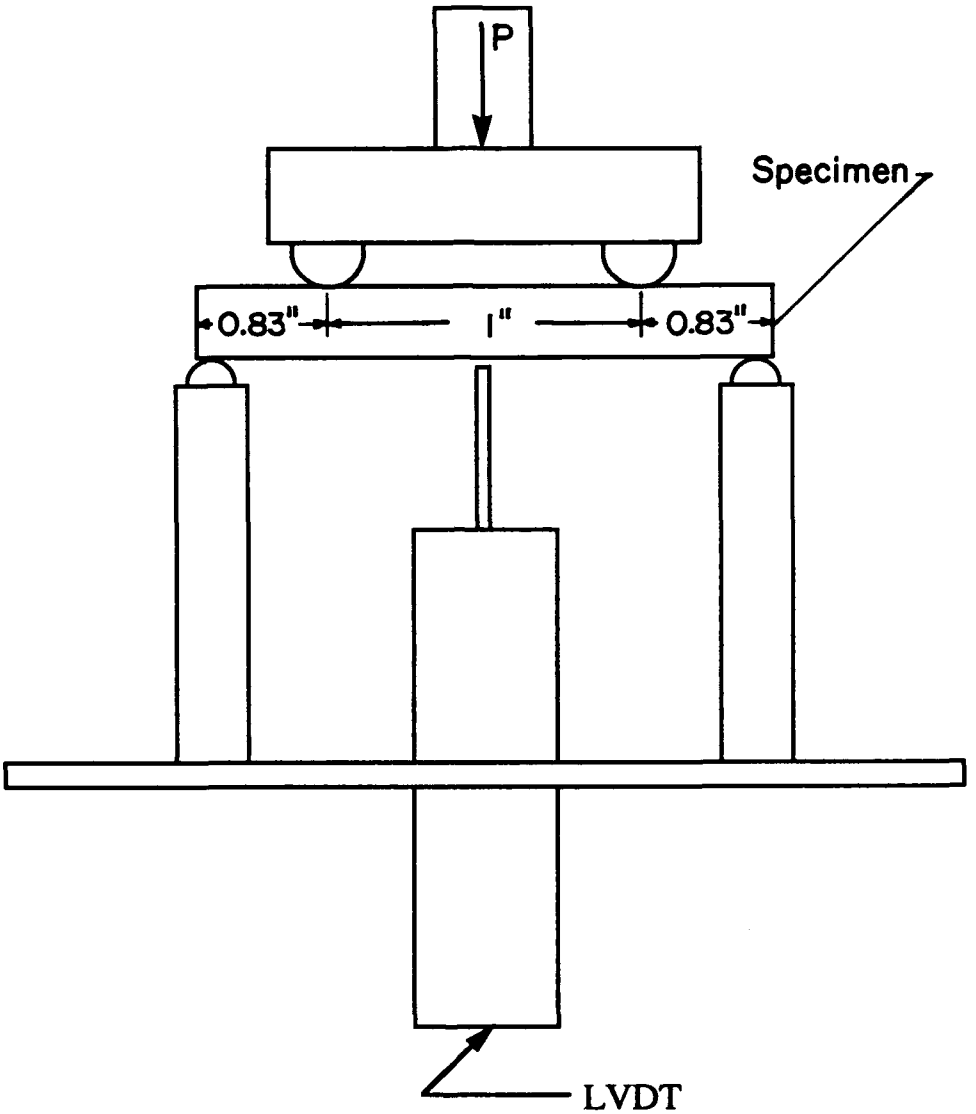

Figure 38
Bending test set up

Applied loads and midspan deflections were measured. From these nominal stresses and strains were calculated based on the elementary strength of materials formulation:

$$S = \frac{M_c}{I} \tag{21}$$

$$\delta_3 = \frac{P\ell^3}{48EI} \text{ (3 point bending)} \tag{22}$$

$$\delta_4 = \frac{P\ell^3}{44EI} \text{ (4 point bending)} \tag{23}$$

In these equations the moment of inertia was based on the minimum cross–section of the specimen and stress concentration was not considered. In Part 2 of this report the data is examined in greater detail with the aid of a finite element program that calculates stresses more accurately. The finite element calculations indicate that failure stresses at the roots of notched specimens are greater than those for unnotched beams, and confirm the existence of a size effect.

Test results are presented in Table 11 and typical load deformation curves are plotted in Figs. 39 and 40.

The specimens displayed a variety of failure modes, as indicated in Fig. 41. Type 1 beams, as expected, generally exhibited the influence of interlaminar shear and failed by a combination of cross–ply fracture and delamination. This type of behavior was observed in both unnotched and notched specimens.

Type 2 beams fractured more or less as isotropic materials. This failure mode is most pronounced in notched specimens with a straight line fracture through the depth. The effects of warp or fill direction influenced the load carrying capacity and not the failure mode.

Table 11. Four Point Bending Test Results

No. of Specimens Tested	Type of Specimen	Max. Load P, lbs	σ_p	Max. Stress S, ksi	σ_s	Modulus E ksi × 10^3	σ_E	Max. Strain ϵ in/in×10^{-3}	σ_ϵ
9	1W	505.9	36.6	15.238	.549	2.468	.1303	6.467	.306
9	2W	493.2	44.9	19.708	.662	2.395	.190	10.079	1.784
9	1F	335.0	5.0	9.198	.190	1.370	.071	9.547	.180
9	2F	288.2	23.1	11.363	.700	1.307	.067	13.759	3.805
9	1WN	288.7	28.2	14.776	1.353	2.551	.001	7.516	.462
12	2WN	250.3	11.9	18.160	.975	2.367	.077	9.938	.174
10	1FN	177.5	9.0	9.098	.532	1.620	.217	11.325	4.649
10	2FN	175.4	3.9	12.977	.510	1.655	.250	13.509	3.002

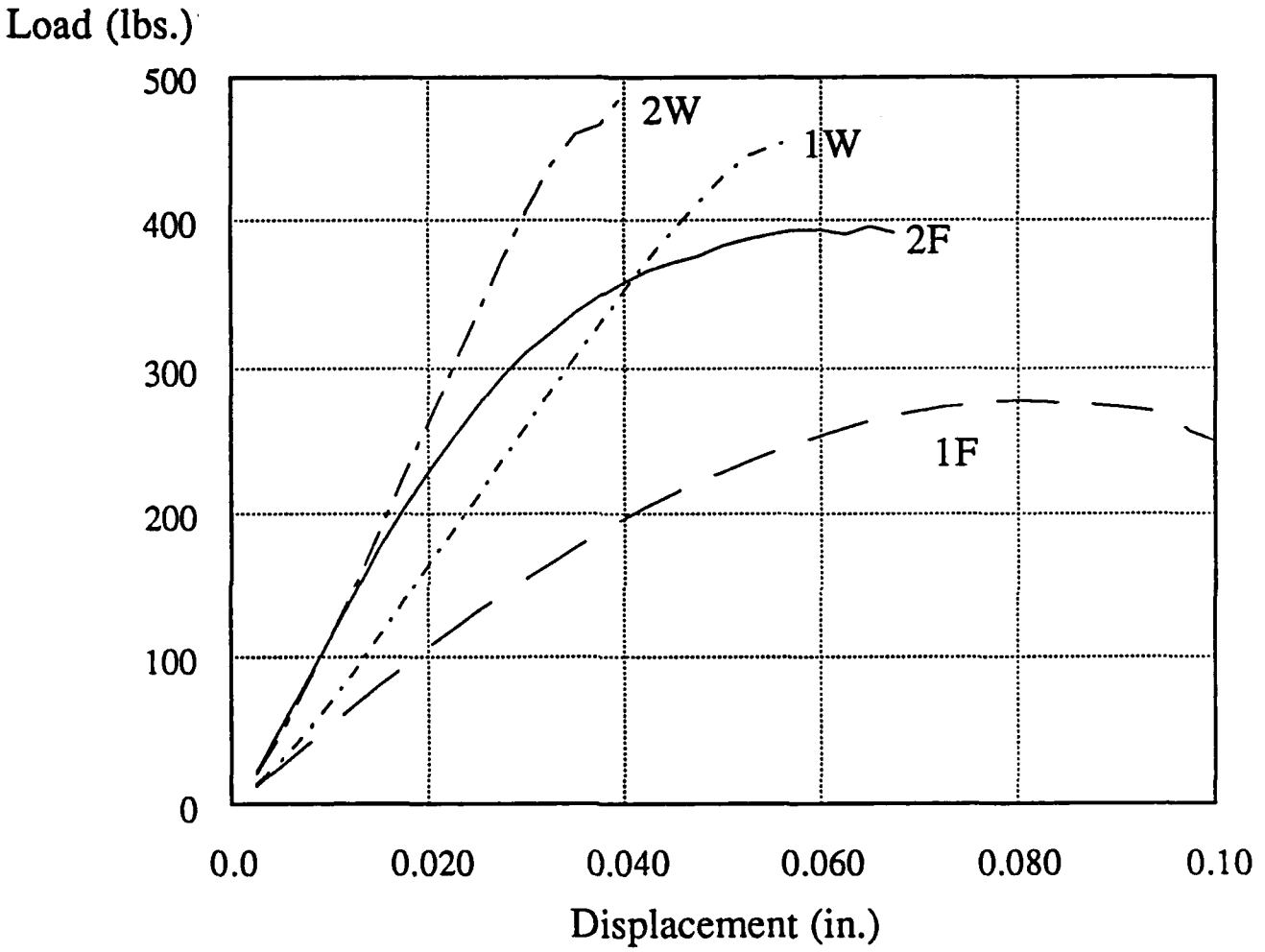

Figure 39
Four print bending load–deformation curves for unnotched specimens.

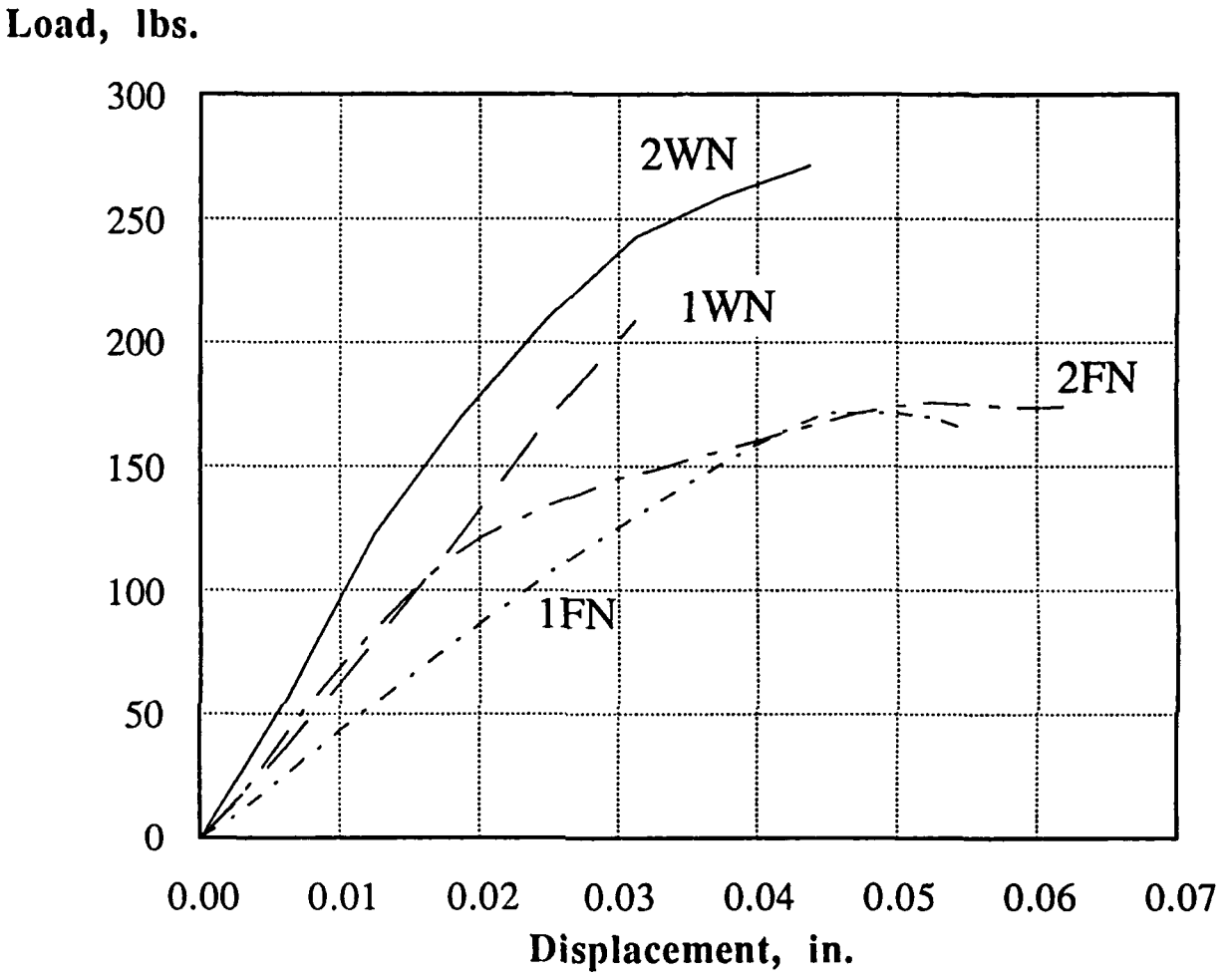

Figure 40
Four point bending load–deformation curves for notched specimens.

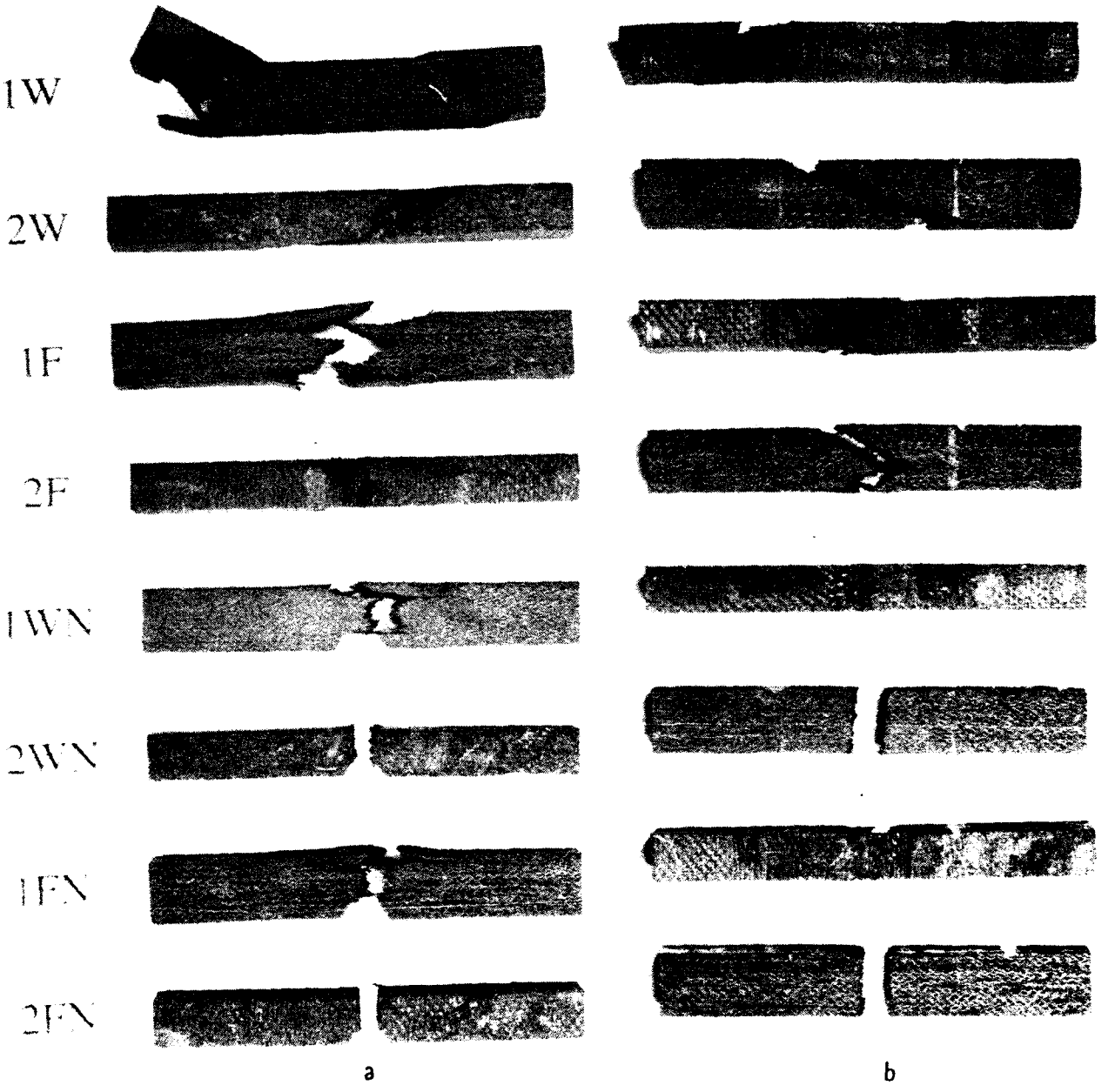

Figure 41
Failed bending specimens a) front view, b) top view.

PLATE BENDING TESTS

As a second method of verifying the size effect concept set forth in Section 12, rectangular and square plates with and without central holes were also tested in bending.

In contrast to laminated beams in which the state of stress is two dimensional, plates must be examined with a three dimensional finite element analysis (Part II of this Report). Such analyses were paralleled by experiments on 9 3/4 × 6 1/2 × 1/2 in. rectangular and 6 1/2 × 6 1/2 × 1/2 in. square plates.

As presented in Fig. 42, plates were instrumented with strain gages placed in the warp (longitudinal) and fill (transverse) directions at the edges of 0.64 in diameter holes and with 0–90° strain rosettes on their diagonals. Similar gauge arrangements were used on a plate without the central hole; here a 0–90° strain rosette was placed at the center of the plate. Additionally, the transverse deflection was measured by a displacement transducer. In some of the tests acoustic emissions were also monitored.

Experiments were carried out on the plate bending fixture illustrated in Fig. 43. Plates were simply supported on all four sides and a uniform load was applied to them through a sand box. To prevent the sand from loading the inner surface of the hole, a central shaft was introduced.

Loads, deflections, and strains on six strain gages were monitored on a multi–channel bridge system and recorded by a computer at five second intervals. Load–deflection curves for rectangular plates are presented in Fig. 44 and load strain curves in Figs. 45–47. Similar data is shown for a square plate with hold in Figs. 48 and 49.

Plate dimensions and maximum loads are tabulated in Table 12. Attempts were made to detect "first ply failures" by monitoring acoustic emission with a transducer placed under the plates. The transducer, however, picked up a great deal of extreneous noise produced by grinding of sand particles, by movement of the simply supported edges and by machine vibrations. As a consequence, the detection of "first ply failure" through these means was not very successful.

A change in the slopes of the nearly linear load–deflection curves was considered to a be a better indication of the onset of significant structural failure, though not of first ply failure.

Strain gauge measurements confirmed the expected results: strains and hence stresses were greatest near the edges of the holes (or at the center of the solid plate) in the fill direction (gauge Q). The square plate exhibited strains nearly as high at the edge of the hole in the warp direction (gage S).

As a consequence, plate failures originated near tne longitudinal diameters of the holes and propagated first along the warp direction, and eventually along the diagonals of the rectangular plates. In the case of the square plate, after originating near the warp diameter of the hole, cracks propagated radially outward.

All plates behaved essentially in a brittle manner; no evidence of delamination was observed.

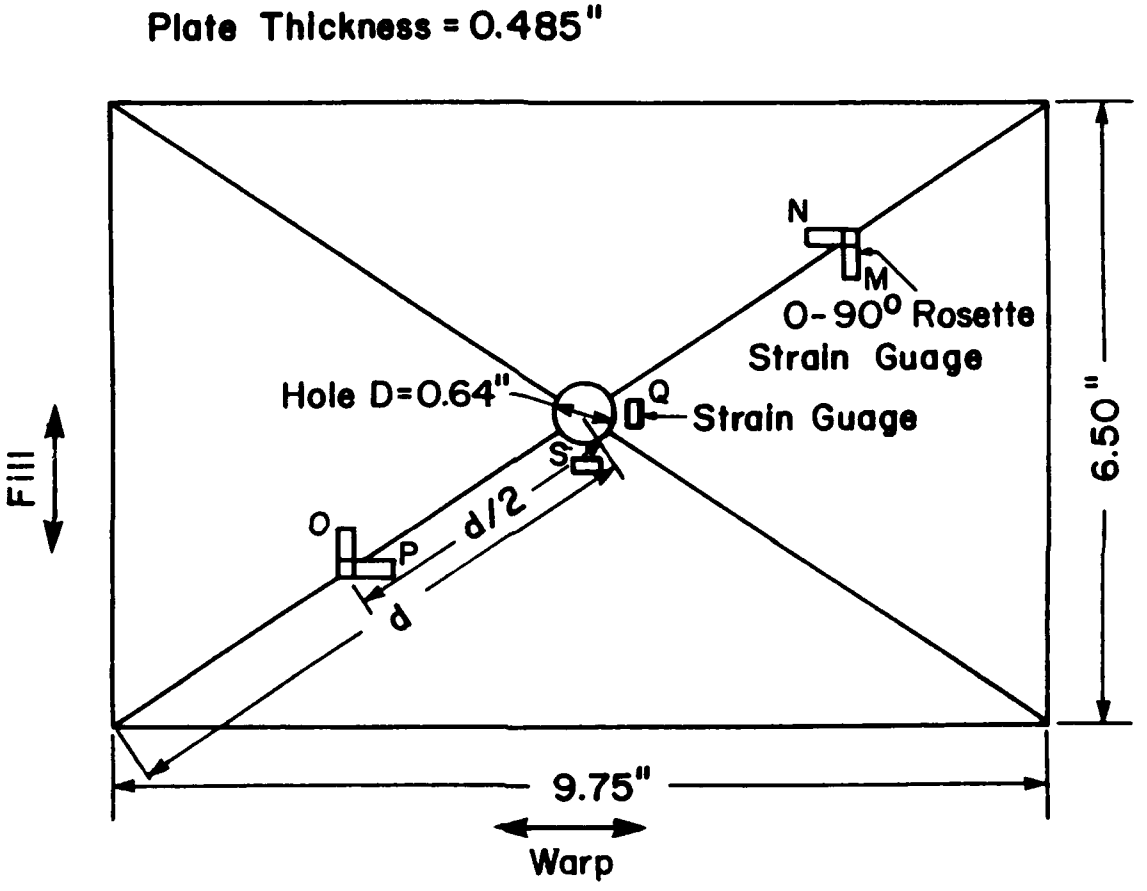

Figure 42
Plate bending specimen.

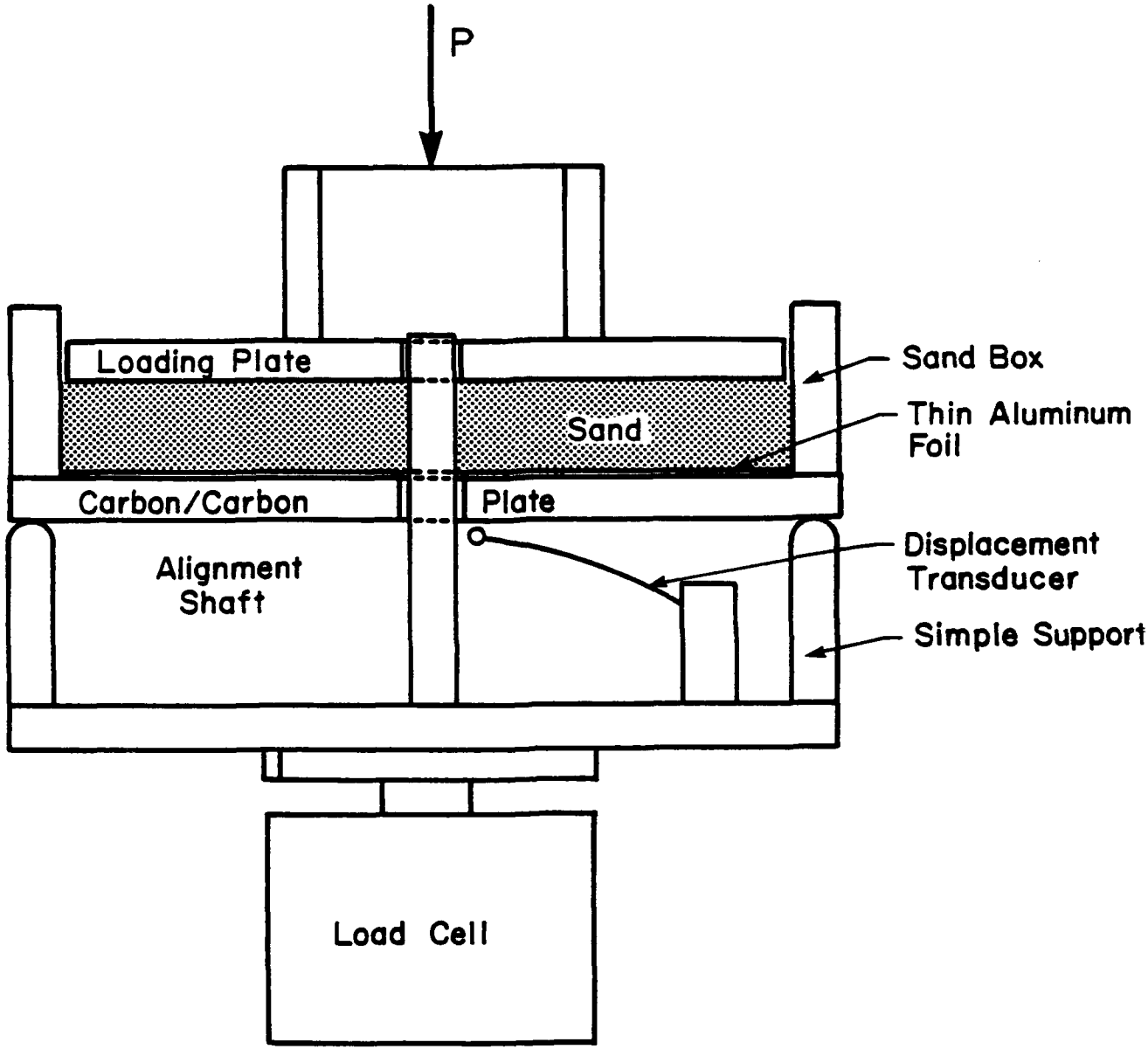

Figure 43
Plate bending test fixture.

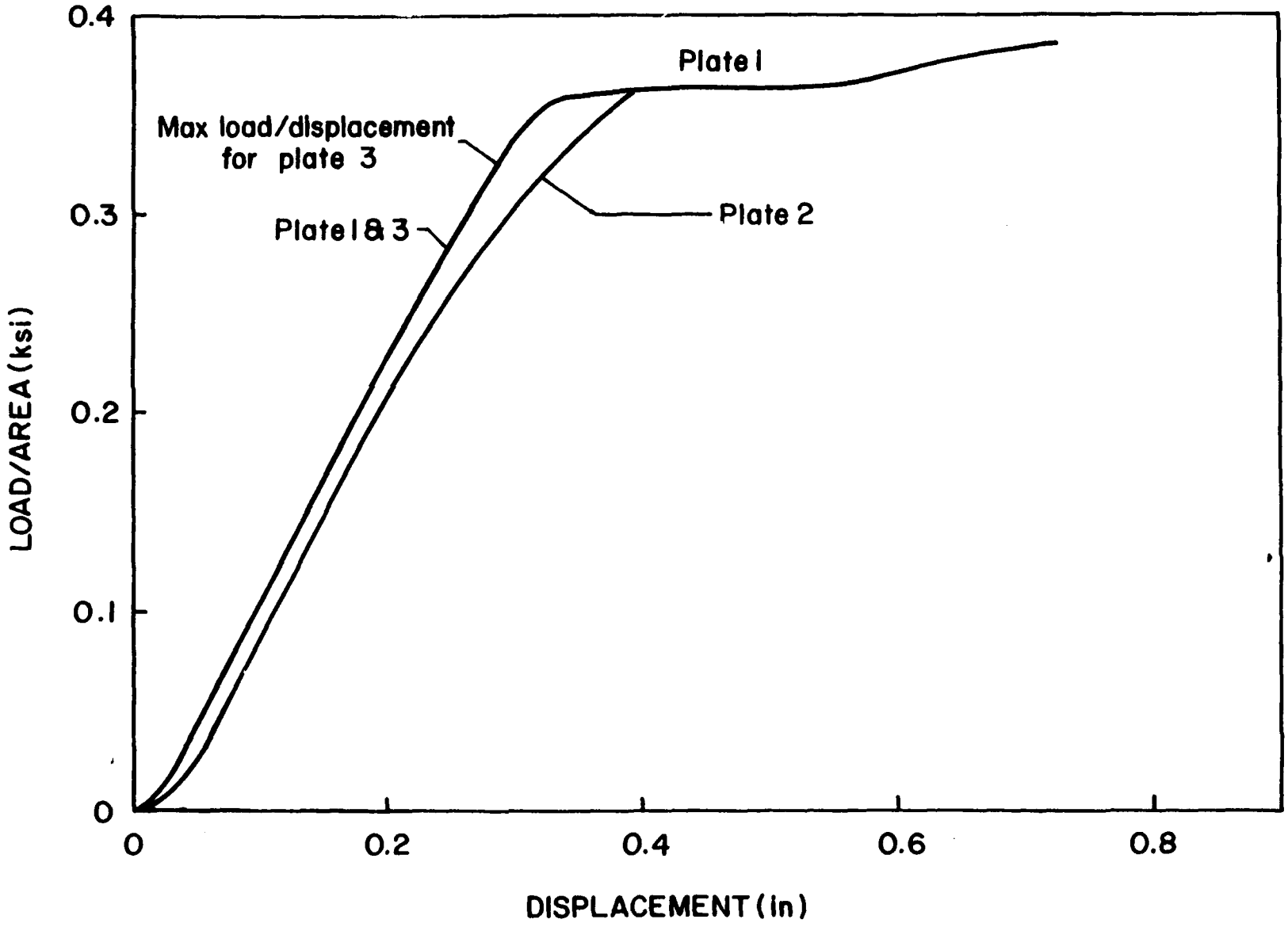

Figure 44
Load–deflection curves for rectangular plates (1 & 2 with hole, 3 no hole).

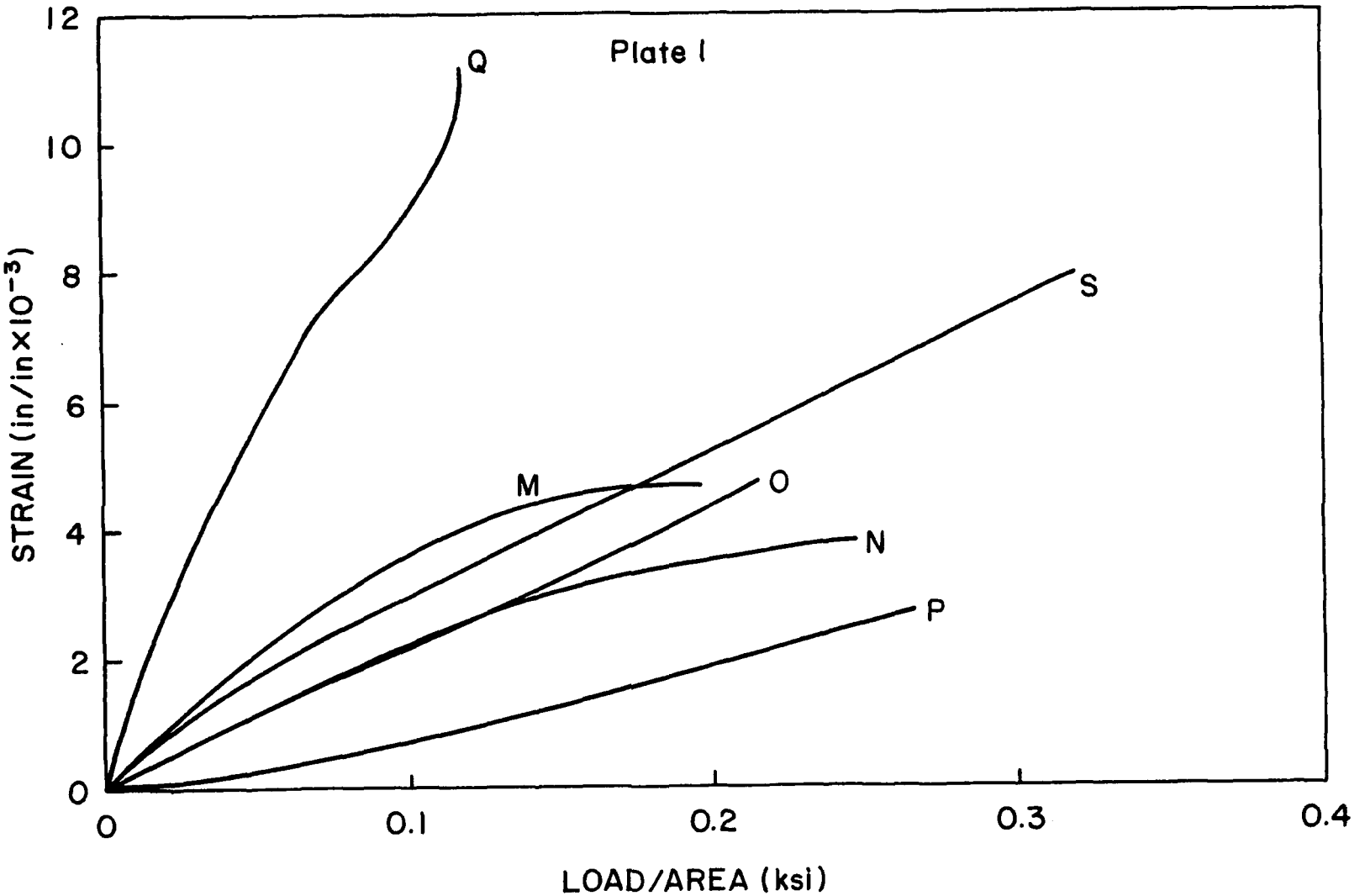

Figure 45
Load–strain curves for rectangular plate 1 (with hole).

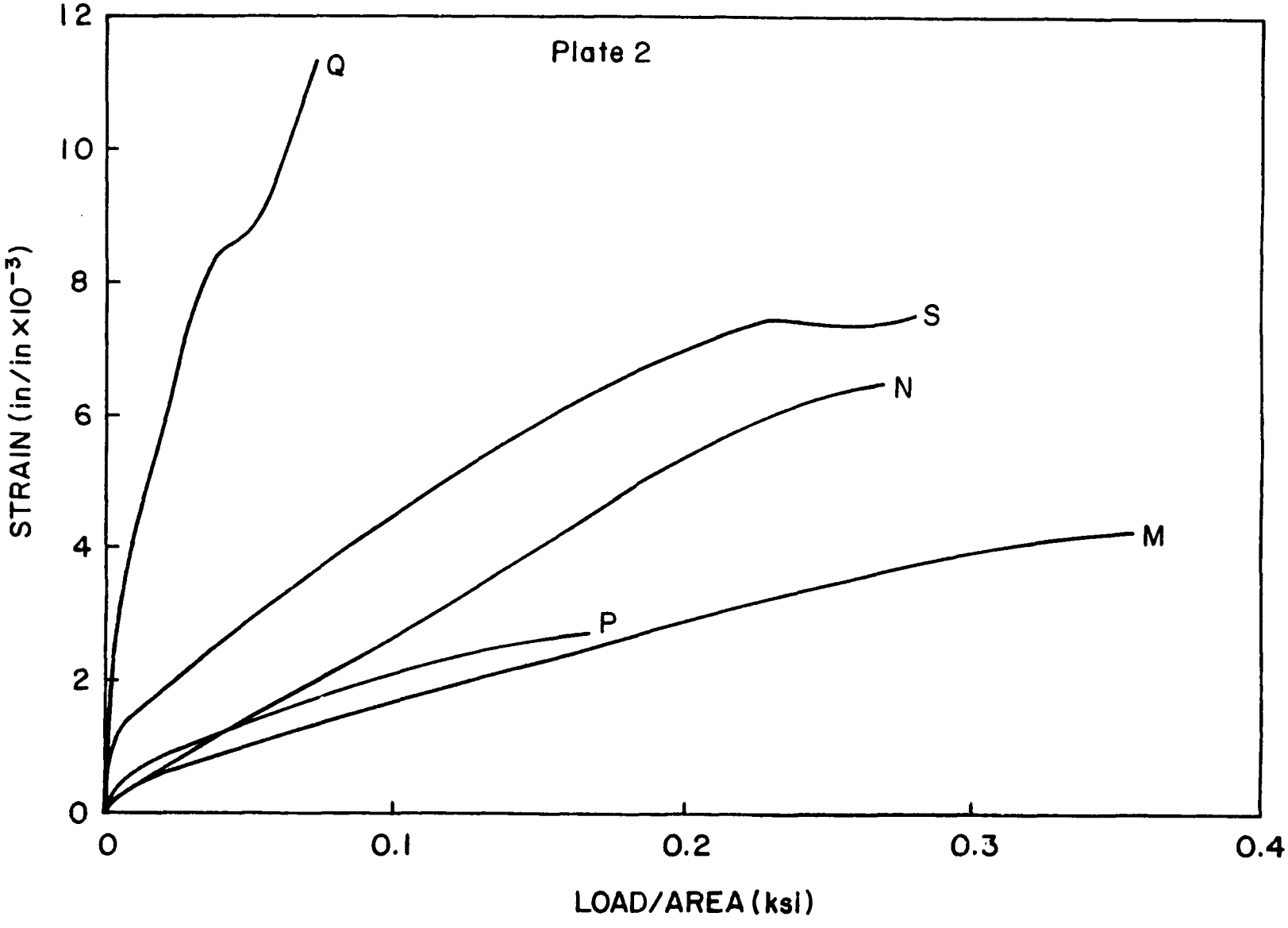

Figure 46
Load strain curves for rectangular plate 2 (with hole).

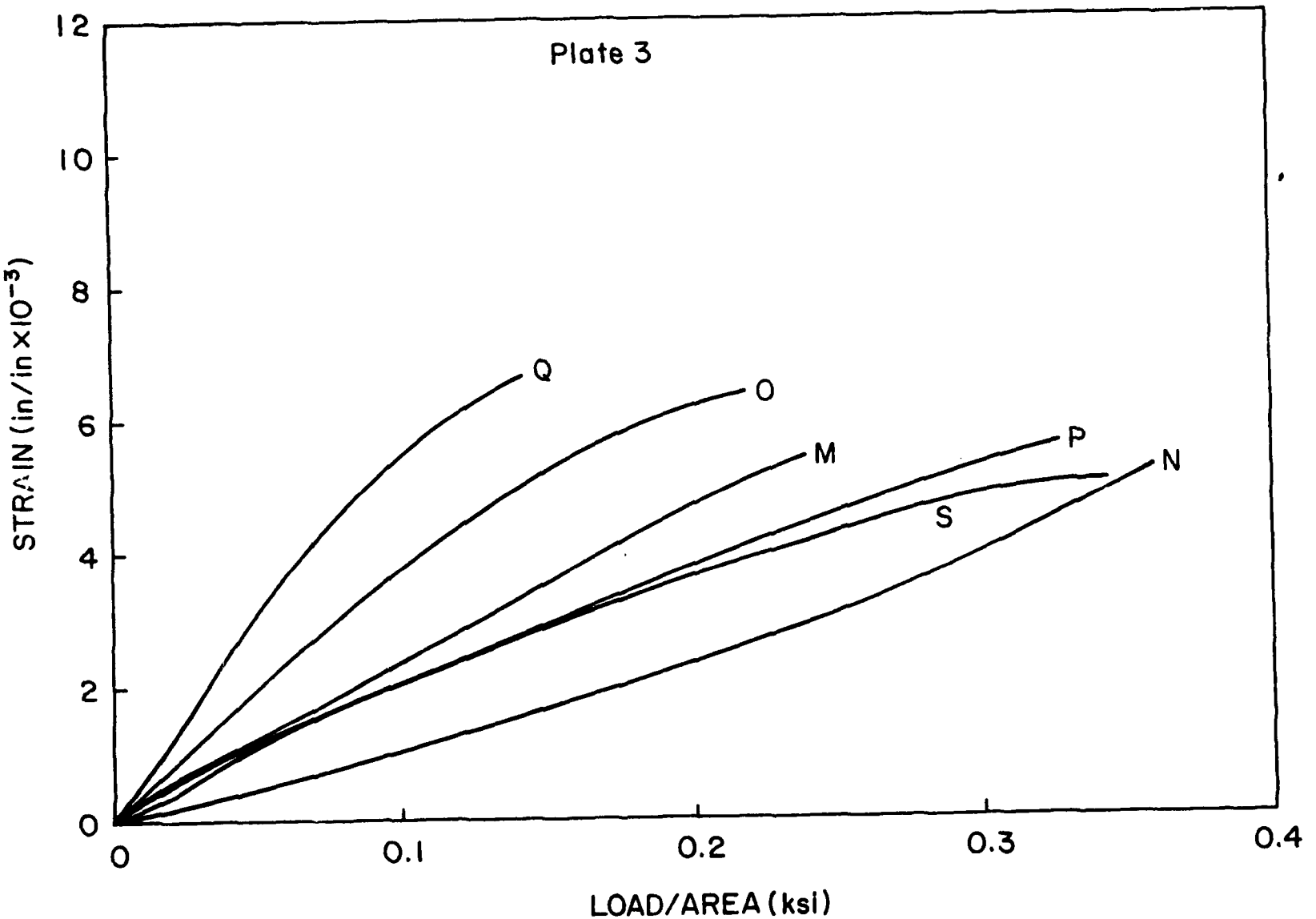

Figure 47
Load–strain curves for rectangular plate 3 (no hole).

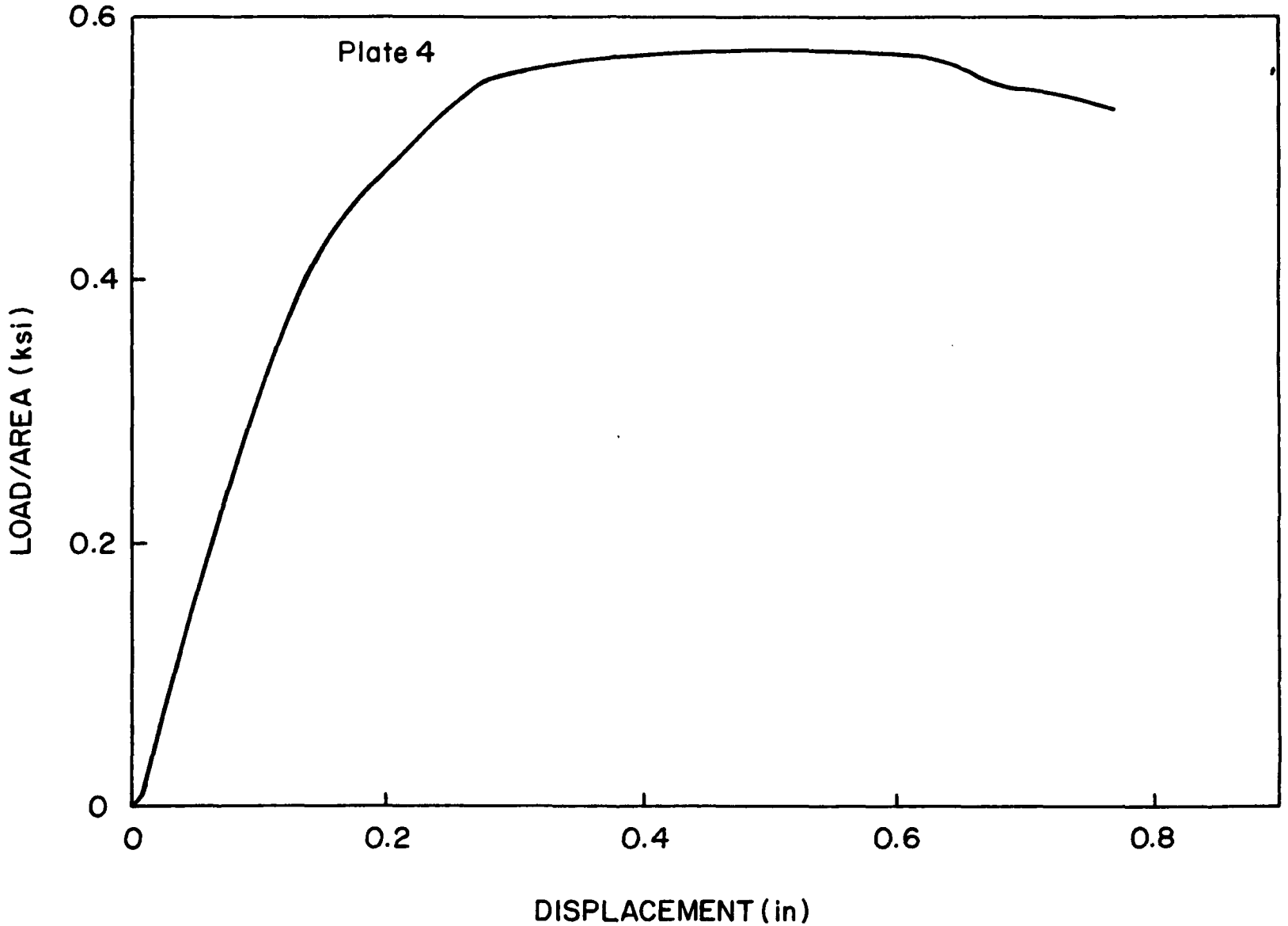

Figure 48
Load–deflection curve for square plate with hole.

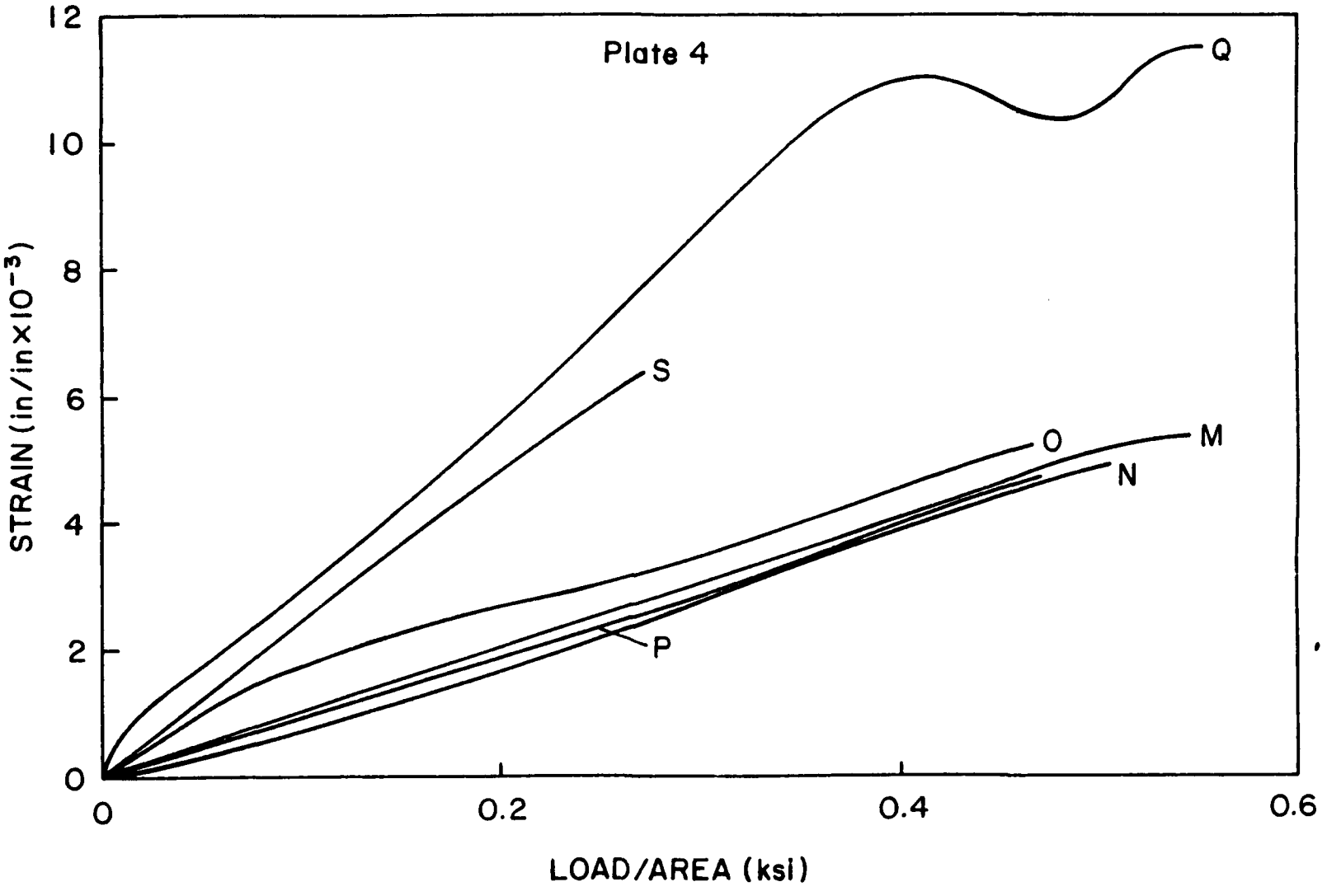

Figure 49
Load–strain curves for square plate with hole.

Table 12. Plate Bending Test Data

Plate No.	Type	Max Load psi	Max. Deflection in
1	*R,H	383	.725
2	R,H	362	.399
3	R,N	360	.286
4	S,H	574	.507

CONCLUSIONS

Mechanical parameters were established for a 2D carbon–carbon composite together with their statistical distributions. These will be utilized in Part II of this report for the analysis of the reliability of beams and plates containing stress raisers and in Part III for the examination of the failure probability of carbon–carbon cylinders subjected to thermal shock combined with internal pressure.

Experiments conducted on beams and plates of this material, also reported here, will be used in Part II a validation of the analytical results.

REFERENCES

1. Rickman, D. K., Davis, H. O., and Wood, G., "Nozzle Material Evaluation. Final Report Air Force Rocket Propulsion Laboratory, AFRPL TR–84–052, August 1984.

2. Pollock, P. B., "Tensile Failure in 2–D Carbon–Carbon Composites," Carbon Vo. 28, No. 5, pp. 717–732, 1990.

3. Lee, H. J., and Heller, R. A., "Propulsion System Hazards and Structural Service Life Prediction," Technical Report U.S. Army Missile Command CR–RD–PR–88–3. November 1988.

4. Snowdon, J. C., "Vibration and Shock in Damped Mechanical Systems." Wiley, New York, 1968.

5. Heller, R. A., Schmidt, A., and Demninghoff, R., "The Weakest Link Concept After Proof Testing." IUTAM Symp. on Probabilistic Methods in the Mechanics of Solids and Structures, Ed. Eggwetz, S., and Lind, N. C., Springer, Berlin, 1985.

6. Guess, T. R., and Bert, C. W., "Material Design Concepts for Filament Wound Graphite–Graphite Heat Sheilds," J. Spacecraft & Rockets, V. 9, No. 3, pp. 165–172, March 1972.

7. Guess, T. R. and Bert, C. W., "Material Design Concepts for Filament Wound Graphite–Graphite Heatshields: Further Analysis." J. Spacecraft & Rockets, V. 10, No. 2, pp. 159–160, 1973.

8. Grose, J. G., Marx, D. A., Norman, J. P., and Jortner, J., "Improved Measurements of Interlaminar Shear Strength in Carbon–Carbon." Symp. on High Temperature Composites, Am. Soc. Composites, June 1989, Dayton, OH.